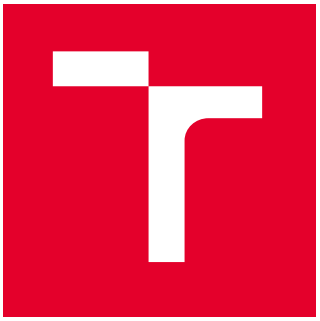

BRNO UNIVERSITY OF TECHNOLOGY

VYSOKÉ UČENÍ TECHNICKÉ V BRNĚ

FACULTY OF MECHANICAL ENGINEERING

FAKULTA STROJNÍHO INŽENÝRSTVÍ

ENERGY INSTITUTE

ENERGETICKÝ ÚSTAV

DESIGN AND OPTIMIZATION OF THE GEOMETRY OF A PERIPHERALLY DRIVEN WATER DRONE DRIVE

NÁVRH A OPTIMALIZACE GEOMETRIE OBVODOVĚ HNANÉHO POHONU VODNÍHO DRONU

BACHELOR'S THESIS

BAKALÁŘSKÁ PRÁCE

AUTHOR — **Tomáš Jakuš**

AUTOR PRÁCE

SUPERVISOR — **Ing. David Štefan, Ph.D.**

VEDOUCÍ PRÁCE

BRNO 2024

BRNO UNIVERSITY OF TECHNOLOGY
FACULTY OF MECHANICAL ENGINEERING

Assignment Bachelor's Thesis

Institut:	Energy Institute
Student:	**Tomáš Jakuš**
Degree programm:	Fundamentals of Mechanical Engineering
Branch:	Fundamentals of Mechanical Engineering
Supervisor:	**Ing. David Štefan, Ph.D.**
Academic year:	2024/25

As provided for by the Act No. 111/98 Coll. on higher education institutions and the BUT Study and Examination Regulations, the director of the Institute hereby assigns the following topic of Bachelor's Thesis:

Design and optimization of the geometry of a peripherally driven water drone drive

Brief Description:

For the movement of small submarines in the form of underwater drones, it is necessary to develop a suitable shape of the propeller. One possibility is to use the concept known as "rim–thruster", where the blades are not located on the central shaft, but instead on the outer ring. The main advantage of this concept, which is mostly used in shipping, is the possibility of current flow through the center of the geometry.

Bachelor's Thesis goals:

The design of the geometry of the propeller with the necessary parameters for driving an underwater drone. Design verified using CFD calculation.

Recommended bibliography:

CARLTON, J. S., 2018. Marine Propellers and Propulsion. 4. Butterworth-Heinemann.

GÜLICH, Johann Friedrich. Centrifugal Pumps [online]. 3. Berlin, Heidelberg: Springer Berlin Heidelberg, 2014 [cit. 2020-09-09]. DOI: 10.1007/978-3-642-40114-5. ISBN 978-3-642-40113-8. Dostupné z: https://www.springer.com/gp/book/9783662518281

Deadline for submission Bachelor's Thesis is given by the Schedule of the Academic year2024/25

In Brno,

L. S.

prof. Ing. Jiří Pospíšil, Ph.D. Director of the Institute	doc. Ing. Jiří Hlinka, Ph.D. FME dean

ABSTRACT

The subject of this thesis is the design and optimization of a water drone propulsion system. By integrating two innovative propeller designs, toroidal and rim-driven, the work aims to enhance the performance and efficiency of the blade stage. The thesis proposes a hybrid solution to marine propulsion in hopes of reducing tip-induced drag and easing the mechanical complexity of the propulsion system assembly. The research follows a theoretical description of the propeller, complemented by an analytical model that predicts the performance of the blade arrangement. The geometry is defined using a set of parameters that are then used in the design stage in an iterative evaluation process to find viable shapes of the blade for further analysis and to find each parameter's impact on thrust and efficiency. The results are then compared with the findings of the CFD analysis. Experimental validation is used to underline the theoretical findings, confirming the potential benefits of the proposed design in underwater applications. The results demonstrate that the design is a strong alternative to rim-driven solutions of present-day UUV propulsion systems, with possible use in the maritime sector.

ABSTRAKT

Práca sa zaoberá návrhom a optimalizáciou vodného pohonného systému špecializovaného na pohon bezpilotných podvodných dronov. Geometria bola inšpirovaná dvoma pokrokovými prístupmi k návrhu lodných lopatiek a to konkrétne toroidnými a obvodovo hnanými lopatkami. Práca navrhuje využiť geometriu zjednocujúcu tieto dva prístupy s cieľom zjednotiť výhody jednotlivých dizajnov v jedinečnom lodnom šróbe ktorý by bol schopný minimalizovať vznik vírivých štruktúr na špičke lopatky ako aj zjednodušiť komplexitu zostavy pohonu. Výskum sa najprv venuje teoretickej rozprave o návrhu vodných lopatiek a faktorom podmieňujúcim ich funkciu a tvar. Po dôkladnej analýze prúdenia v lopatkovej mreži je odvodený analytický model slúžiaci na odhad ťahu a momentu (ergo účinnosti) návrhu nového tvaru lopatiek. Pre zjednodušenie výrazov je geometria opísaná množinou bezrozmerných parametrov ktoré jednoznačne popisujú výsledný tvar lopatiek. Mnohé z týchto parametrov sú už ustálené v literatúre no boli zavedené i parametre popisujúce práve tvar toroidného obvodovo hnaného pohonu. Tieto parametre sú následne použité pri popise geometrie v procese iteratívneho vyhodnocovania charakteristík lopatiek a postupného hľadania citlivosti systému na odozvu voči zmene jednotlivých parametrov. Pre tento proces bolo využité počítačové modelovanie prúdenia (CFD). Pre validáciu výsledkov z počítačového modelovania bola vykonaná séria meraní v ktorej bola zároveň meraná aj odchýlka jednotlivých modelov. Merania ukázali silné prepojenie teoretických a praktických výsledkov čo sa týka účinnosti (teda implicitne i ťahu a momentu). Zároveň bolo ukázané, že navrhovaná geometrie vie konkurovať moderným pohonom podvodných dronov ako i niektorým riešeniam lodných pohonov.

KEYWORDS

Underwater Unmanned Vehicles, Remotely Operated Vehicles, Rim-driven thruster, Toroidal propeller, Hybrid propeller design, Marine propulsion systems, Propeller geometry optimization, Computational Fluid Dynamics, Blade element method, Cavitation reduction, Thrust efficiency, Deep-sea exploration drones, Autonomous underwater vehicles

KĽÚČOVÉ SLOVÁ

Podvodné bezpilotné vozidlá, diaľkovo ovládané vozidlá, obvodovo hnané vodné pohony, toroidné lodné šróby, návrh hybridnej vrtule, lodné pohonné systémy, optimalizácia geometrie lodného šróbu, výpočtová dynamika tekutín, metóda lopatkových prvkov, zníženie kavitácie, účinnosť ťahu, preskumné drony, autonómne podvodné vozidlá

CITATION

JAKUŠ, Tomáš. *Design and optimization of the geometry of a peripherally driven water drone drive.* Brno, 2025. Available also at: https://www.vut.cz/studenti/zav-prace/detail/162340. Bachelor's Thesis. Brno University of Technology, Faculty of Mechanical Engineering, Energy Institute. Supervised by Ing. David Štefan, Ph.D..

AUTHOR'S DECLARATION

I declare that this thesis is my original work, I have created it independently under the supervision of my thesis supervisor using literature and other sources of information, all of which are cited in the thesis and listed in the reference list.

As the author of this thesis, I further declare that in the context of creating this thesis, I have not infringed the copyright of third parties, in particular, infringement in an unauthorized manner on the personal copyright of others, and I am fully aware of the consequences of violating the provisions of Section 11 et al. of the Copyright Act No. 121/2000 Sb., including possible criminal consequences.

In Brno on 20. 5. 2025

Tomáš Jakuš

ACKNOWLEDGEMENT

I would like to express my sincere gratitude to Ing. David Štefan, Ph.D. for his invaluable guidance and patience throughout the preparation of this work. His expertise in the field of turbo machinery and computational fluid dynamics has proven invaluable when addressing the numerous challenges related to this research. His feedback has significantly affected the quality of this work.

The appreciation also extends to the members of the fluid flow laboratory at the Victor Kaplan Department of Fluid Engineering, Brno University of Technology. Namely Ing. Martin Hudec, Ph.D. and Mr. Bronislav Kusý for their assistance and suggestions when conducting the experimental measurements.

Rád by som vyjadril úprimnú vďaku Ing. David Štefan, Ph.D. za jeho vedenie a trpezlivosť počas tvorby tejto práce. Jeho znalosti v odbore lopatkových strojov a CFD sa ukázali byť nesmierne nápomocné pri riešení mnohých problémov ktoré sa na ceste k výsledkom vyskytli. Jeho spätná väzba mala neoceniteľný dopad na kvalitu tejto práce.

Moja vďaka patrí i členom výskumného laboratória ústavu fluidného inžinierstva Viktora Kaplana, VUT v Brne. Najmä Ing. Martinovi Hudecovi, Ph.D. a Bronislavovi Kusému za ich návrhy a asistenciu počas vykonávania meraní v tejto práci.

CONTENTS

INTRODUCTION

The recent development of Underwater Unmanned Vehicles (UUVs), more commonly placed in the category of Remotely Operated Vehicles (ROVs), allowed mankind to broaden its knowledge in deep-sea explorations and enabled it to save lives while minimizing the risk of additional casualties. It became common practice for oceanographers to deploy UUVs in deep-sea explorations and seafloor mapping missions. In Rotterdam, the fire brigade disposes of underwater sonar-equipped UUVs used to locate victims in murky waters to aid rescuers. [8] Another example of the application of UUVs was the Tham Luang cave disaster in June 2018. Operatives considered the use of UUVs to map underwater terrain to better guide divers during the rescue mission, however, the mission was later called off due to dangerous conditions even for unmanned vehicles. [10] This serves as an example of how much there is still to improve on this design and how helpful drones can be as soon as we perfect them. The recent onset of UUV application has accelerated its design and led to many breakthroughs in its design and use.

Three years ago a student team, based at Brno University of Technology, set off to design a UUV capable of deep underwater exploration with the ultimate goal of discovering and mapping the bottom of the second deepest flooded pit cave in the world situated in the Czech Republic, the depth of which remains unknown to date. The deepest estimate is over 450 meters, but is speculated to be much deeper. So far no diver or drone has discovered the bottom due to the complex and dangerous system of underwater flooded caves. [4] The team's efforts are to design a drone durable and complex enough to be able to map the cave and proceed to its deeper levels autonomously. [5] This thesis focuses on designing the propeller with which the drone will be equipped. The efforts have led to exploring modifications of modern designs used in tankers, adjusting to the specific application, and assessing their performance in this application.
This thesis lays down the basic concepts of how to combine two different successful propeller geometries, namely the toroidal and rim driven propeller. In the following chapters, the geometry for all three, conventional, toroidal, and rim driven thrusters will be described along with equations and characteristics governing their operation derived. From there, a description of a hybrid toroidal rim driven thruster will be carried out, the model will be later assessed using a mathematical model, and undergo a preliminary parametric study to obtain initial values for geometry parameters. The findings from this model will be converted into a three-dimensional geometry and iteratively re-evaluated in a commercial CFD code to explore the variable space describing the surface of the blade and its impacts on the performance. Finally, the results will be validated in laboratory experiments to validate the theoretical findings.

1 LITERATURE OVERVIEW

The history of marine propulsion dates back to Archimedes and his screw propeller in 250 BC. From there, development in the form of Da Vinci's drawings of propellers in the sixteenth century can be seen. The first propeller design with features that are recognizable today comes from Robert Hooke, who was better known for his law on the mechanics of materials. The story unfolds with names that are well recognized today, such as Kirsten-Boeing, Bernoulli, Euler, Taylor, and Napier. Eventually converging to Robert Griffiths' design from 1860, he invented the screw propeller used today. [14]

In 1939, Friedrich Honerkamp issued a patent for a propeller design that folds the propeller blades onto themselves, claiming a reduction in noise and turbulence. He named the shape a toroidal propeller. [16] Not so long later, engineers began to experiment with new technology in aviation and marine applications. To date, 170 patents have been issued under the common category of propellers, where 'each blade is constituted by a surface that covers an empty space, for example, forming a closed loop.' [1] [31] This concept was revisited in 2017 when researchers from the Massachusetts Institute of Technology developed and patented a toroidal drone propeller that claimed to shift generated sound waves to higher frequencies where human hearing is not so noticeable, thus making it sound quieter. [32]

This initiated a new phase in propeller design advancements, leading to explorations of shapes that showed potential for superior performance compared to current propulsors. Yue Xiang [36] evaluated the performance characteristics of a conventional and toroidal propeller under the same conditions (5000 RPM) and showed that a submarine equipped with a toroidal propeller can exceed the speed limits of the same vessel propelled by a screw propeller. Although supporting evidence is limited, experiments have repeatedly shown the superiority of toroidal propellers over commercial designs. One of the best examples is the Sharrow Marine propeller [33], which is a commercially available positive rake toroidal propeller patented and introduced to the market in 2024. Third-party tests claim that it increases vessel fuel efficiency by up to 46% [9]. The Sharrow Marine MX line was awarded as the best propeller of the year in 2023 and 2024 by the Times Magazine [6]. The key to success lies in a mechanism similar to airplane winglets that eliminate induced drag by reducing the vorticity created by high pressure medium 'leaking' around the tip of the wing, causing circulation that manifests itself as induced drag and propagating downstream turbulence [11]. Similarly, toroidal blade design purges the tips by merging individual blades in hopes of eliminating tip-induced drag.

During the same time, a second revolution in marine propulsion has been underway. Following the development of podded propellers in 1931, three years later, Ludwig Kort proposed his newly improved Kort nozzle design along with the suggestion of completely

[1] Patent category B63H1/265

removing the central shaft to ease the mechanical complexity of the assembly and allow for a slimmer and more efficient application. Today, commercial versions of this design are available from manufacturers such as Rolls Royce under the commercial name 'permanent magnet tunnel thruster' [7]. This design is commercially recognized as rim-driven thrusters or rim-driven propellers. Its uses are viable anywhere where a conventional podded propeller would be used. Azimuth thrusters and bow thrusters are commonly used in marine vessels and in UUVs [37], with rim driven counterparts that use increased performance and environmental sustainability due to their reduced noise generation, longer durability, and overall lower assembly complexity. The concept behind the rim thruster was to eliminate the interference between the tip of the propeller and the stationary nozzle. The researchers effectively prevented cavitating vortices from leaking into the intermittent space between the blade and the shroud and flowing downstream by integrating the tip into the nozzle and allowing the shroud to rotate with the blade. With up to 40% less chance of cavitation in higher numbers of blades (5-6 blades). [17] As Zhipeng and Houlin [41] point out, this can lead to an increase in thrust by up to 20% and an overall efficiency by 15%. The consistent pattern among research remains that rim driven thrusters purge unwanted tip vortices and minimize the risk of cavitation as well as allow for quieter and more efficient operation. Another advantage of removing the central hub of a propeller is the creation of a cavity that allows any debris such as ropes, fishing lines, or trash to fly through the propeller instead of being tangled in the shaft [39].

A demonstration of the promised performance of rim thrusters can be seen in commercially available products on the market. One of the most successful companies is Copenhagen Subsea [3], which markets rim thrusters claiming improved thrust, efficiency, and durability properties.

The logical progression in this line should be (and is a subject of this thesis) to attempt combining both designs into a rim driven propeller with its tips connected into an annular surface to minimize turbulence generated on the inner tips of the blades and eliminate outer-tip-induced drag as well as any cavitation formed on the outmost point of the tip.

1.1 Fixed Pitch Propeller Geometry

In this chapter, a variant of screw propeller geometry with its blades fixed to the central hub without the ability to change its pitch should be analyzed, as this is the most common design and will be employed later in this work to derive the new geometry.
Before describing any geometry, it is important to provide definitions for propeller elements. In marine propeller engineering, the standard nomenclature follows that established by the International Towing Tank Conference [15]. The following sections utilize the terminology established at the 22nd Towing Tank Conference held in 2008, along with the geometry descriptions provided by John Carlton [14].

A shroud, or duct, is a concentric stationary part around the propeller that is used to accelerate (Kort Nozzle) or decelerate (Pump jet) the stream passing through the propeller stage. Sometimes, the duct is used to direct the flow of water behind the propeller stage or as a protective element in some cases, specifically in UUVs to protect any nearby personnel and the environment. Although ducts generally feature elliptical sections, the exact form of a propeller can enhance tugboat performance by up to 30%. For the purposes of this thesis, a cylindrical duct is assumed, concentric with the rotation axis, as the shape optimization of the duct exceeds the scope of this work. A hub is a part of the drive shaft to which the blades are attached. This part lies on the rotational axis of the propeller.

The coordinate system of a screw propeller is shown in Figure 1

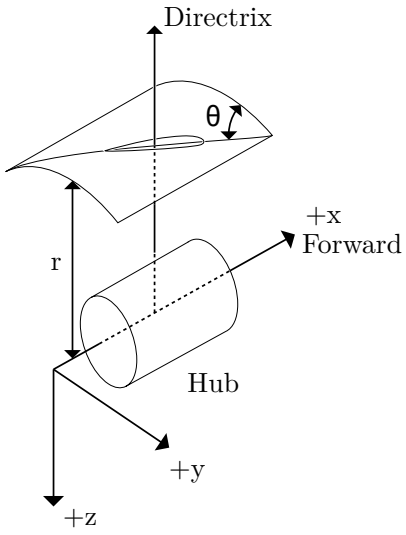

Figure 1: Screw propeller coordinate system, adapted from [14]

The positive x axis is defined as pointing toward the bow of the vessel, with the arbitrary exception of hinged podded thrusters. The y direction is oriented towards the ship's starboard. Then the positive z axis must point downward to form a right-handed coordinate system. To create a surface of the propeller blade, the hub must be defined first as a cylinder with a radius of r_{hub} from the center of which at an angle of ϕ to the plane of YZ and normal to XY is defined as the directrix of the blade section. For every radius $r \in [r_{hub}; r_{rim}]$ a concentric cylinder with the x axis, where r_{rim} is the radius of the outmost point. Let a chord line be defined as a section of a helix curve with radius r and length c such that the center of the helical section lies at the intersection of the directrix and the radius cylinder r. This parameter c is called the chord length of a section. The pitch p of the helical section is the same as that of the helical curve, thus the distance traveled in one full revolution around the x axis.

$$p = \frac{\Delta x}{2\pi r} \tag{1}$$

A complimentary angle θ is the pitch angle of the helical section:

$$\tan(\theta) = \frac{p}{2\pi r} \tag{2}$$

The cylindrical section is a blade section defined on the cylinder such that the nose and the tail of the section coincide with the endpoints of the cylindrical section. The blade cross section is traditionally a NACA profile, an elliptical profile, or a general closed loop. As a deviation from the nomenclature, let there be another curve defined as the center line that passes through the centroid of all intersections between the directrix and the cylinder for all values of r and be labeled γ or a *center line*.

Alternatively, the cylindrical section can be defined using a cross section in a plane normal to the directrix at a distance r from the x axis with a center line of length c centered on the intersection and at an angle of θ with the yz plane. The cross section is then projected onto a cylinder of a radius r using conformal mapping. [28] The surface of the blade is constructed by joining all cylindrical sections for each radius from hub to shroud, while the individual sections can vary in their orientation (θ) and size (c). This is defined using blade geometry functions, that is, in the variation of chord length and deviation of the directrix from $-\hat{z}$ as a function of r. Thus, leading to the definition of functions $c_{(r)}$ and $\phi_{(r)}$. If the angle $\phi_{(r)}$ is linear through the entire definition with respect to r, we say that the blade is *skewed*. Another commonly defined property is the rake of a propeller. This value is introduced when the directrix does not lie in a plane coplanar to yz but is tilted by an angle of φ. This angle is then labeled as a propeller rake.

1.1.1 Blade Cross Section

The blade cross section can be defined as any closed curve that contributes to the surface of the blade. The shape is commonly an airfoil for aircraft propellers and a hydrofoil for marine applications. Alternatively, an elliptical or any other section can be defined. The most effective have proven to be sections defined by the National Advisory Committee for Aeronautics, shorthand for NACA (presently recognized as NASA). The profile is defined by a chord line of length c connecting the start (leading edge) and the end (trailing edge) of the chord line following a pre-defined curve, the camber line. The maximum camber of a cross section is then the maximum distance between the camber line and the chord line. A series of circles centered on each position of the camber line then define the envelope of the cross section creating an upper and a lower surface of the cross section that is symmetric about the camber line. The conventional NACA four-digit series characterizes the airfoil by utilizing three parameters. The first digit indicates the maximum camber as a percentage of the chord length. Subsequently, the second digit indicates one-tenth of the distance from the leading edge to the point of maximum camber. Finally, the last two digits specify the maximum thickness of the airfoil, which is also expressed as a percentage of the chord length. [21]

For reasons described in Section 3.4, the only relevant NACA airfoils suitable for the investigated designs are symmetrical variants where the camber line is identical to the

chord line, thus producing a section symmetric with the local x axis. Hence, the four-digit code is $00xx$ and the only relevant parameter remains the percentage of the maximum thickness along the chord. A symmetrical four-digit NACA airfoil can then be described by the following equation:

$$y_t = 5t(0.2969\sqrt{x} - 0.1260x - 0.3516x^2 + 0.2843x^3 - 0.1015x^4) \tag{3}$$

With y_t being the y coordinate of the envelope, t one-hundredth of the maximum thickness of the airfoil (the two last digits) and x a chordal position parameter $x \in [0; 1]$. [1]

Alternatively, the airfoil can also be an ellipse of a given thickness passing through the leading and trailing edge of the chord line.

The performance of a given cross section is characterized using experimentally obtained coefficients of lift and drag that relate to Lift ($+\hat{x}$) and Drag (tangential) forces on the airfoil with the following relations:

$$L = \frac{1}{2} C_L \rho S v^2 \tag{4}$$

$$D = \frac{1}{2} C_D \rho S v^2 \tag{5}$$

$$S = t \times c \tag{6}$$

where
L is Lift force
C_L is coefficient of lift
C_D is coefficient of drag
ρ is medium density
S is wing surface area
v is incident velocity
t is wing length

Note that lift and drag coefficients are dependent on the angle of incidence α of the airfoil and are best characterized by their ratio as a function of α:

$$\frac{C_L}{C_D}_{(\alpha)} \tag{7}$$

The maximum of this ratio is the most efficient angle of incidence where the airfoil produces the most lift compared to its drag, this angle is referred to as α_0. When designing a propeller, to achieve the best efficiency, the airfoil section should be rotated such that the incident flow collides with the airfoil section at an angle of α_0.
To obtain the angle of incident flow, the concept of velocity triangles is introduced. In a rotating reference frame, the magnitude and direction of incident velocity in the airfoil

must be the sum of the tangential and axial velocity. The tangential velocity introduced by the rotation of the blade is:

$$\vec{v} = \vec{\omega} \times \vec{r} \tag{8}$$

The axial velocity is the effect of the propeller operation, alternatively, by the movement of the vessel. In the case of cargo ships, it is said that the axial velocity is roughly equal to the velocity of the ship, in the case of tugboats, the axial velocity is the x component velocity induced in the propeller stage [14]. Now, the angle θ from the equation. 2 can be modified to:

$$\tan(\theta_{(r)}) = \frac{(\Delta x)'}{(2\pi r)'} = \frac{u_{(r)}}{v} \tag{9}$$

A visual representation if the vectors is featured in figure 2. Another phenomenon in propeller action is the effect of the induced angle of attack. Due to vorticity effects on the trailing edge of the propeller, the flow is diverted downwards and causes induced drag and reduced thrust. The effect of induced flow on the wing can also be described as if the incident flow had been diverted by an angle of α_i in addition to θ [12]. Armin Ghoddoussi [18] in his Ph.D. thesis describes an equation to calculate the induced angle of attack.

$$\alpha_i = \frac{1}{2}\left(-\left(\frac{v}{u} + \frac{\sigma a v_R}{8x^2 v}\right) + \left(\left(\frac{v}{u} + \frac{\sigma a v_R}{8x^2 v}\right)^2 + \frac{\sigma a v_R}{8x^2 v}(\alpha_0 - \theta)\right)^{\frac{1}{2}}\right) \tag{10}$$

where σ, x, v_R are parameters such that:

$$\sigma = \frac{Bc}{\pi r}; x = \frac{r}{r_{rim}}; v_R = v\sqrt{x^2 + \frac{1}{cos^2(\theta)}}; a = \frac{dC_L}{d\alpha} \tag{11}$$

Where B is the blade number.

Bearing this in mind, it is possible to define the position at which the blade section will be optimally oriented. Angle β is defined as the propeller advance angle and is equal to the pitch angle θ and β_I represents the hydrodynamic flow angle, which is the inflow angle of the blade section including the induced velocities and section angle of attack [15]. The following figure shows the relationship between the individual angles discussed in this chapter.

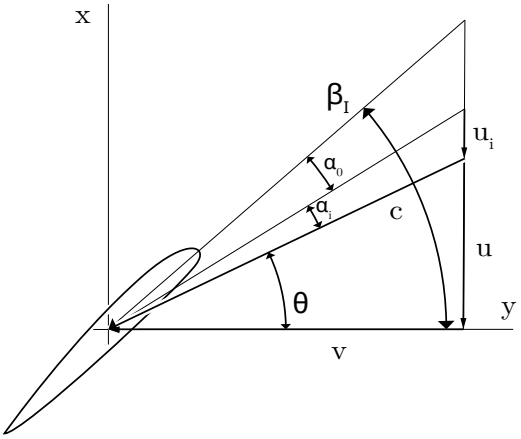

Figure 2: Blade angles adapted from [14]

As can be observed in figure 2, it is best to rotate the blade section at an angle of β_I with respect to the xz plane. And for the value of β_I:

$$\beta_I = \theta + \alpha_0 + \alpha_i \tag{12}$$

1.2 Toroidal Propeller Geometry

As mentioned before, an annular approach to propeller geometry is a new and unexplored variation with very little research available. This chapter adopts some assumptions and techniques used by Liyu YE et al. [40] who developed a mathematical description of the toroidal propeller. The premise of creating a toroidal surface propeller is similar to the one of designing an airplane wing tip with an annular shape to mitigate parasitic vorticity generated at the most distant point of the blade. This approach reduces the tip-induced drag and improves the lift-to-drag ratio of an aircraft wing by up to 7% [19]. For the same reasons, it was assumed that by modifying the propeller center line to form an annuloid, the tip vorticity can be reduced and overall performance improved [31]. Liyu YE et al. further describe another mechanism taking place and that is when the two blades operate as co-rotating tandem propellers and the second in the series has a staggered position and different angle β_I to account for the flow changes imposed by the first propeller in the series. In tandem, they operate as one propeller blade with an expanded blade area encompassing both blades. The design procedure is analogous to the one of a fixed pitch propeller; however, special functions describe the rake and skew profiles. Another problem emerges at the midpoint of the propeller, which functions as the transition point between the two blades and represents an inflexion point when defining any of the geometric features. For this point, a special approach is taken, and the blade surface is defined using a center line as suggested in Section 1.1.

1.3 Rim driven propeller geometry

The design process of a rim-driven propeller follows concepts similar to those used in fixed-pitch screw propeller geometry with the deviation of the absence of the central hub from the geometry (and the drivetrain). The root of the blade is defined at $r = r_{shroud}$ and is advanced inward in the direction of $-r$. The interaction between the blade and the shroud is reduced due to the absence of tip leakage. This improves overall performance and allows for a better use of the shape of the duct itself [25]. The design contributes to a more compact assembly and eliminates the need for bends in the inlet and outlet ducts, removing the need for various pipe configurations to circumvent the central shaft motor seen in applications such as jet propulsors. [30]

2 PROBLEM FORMULATION

Before proceeding further, it is necessary to define the objective of the design and its application. As discussed earlier, the propeller proposed in this thesis is to be fitted onto a UUV tasked with deep underwater exploration in murky waters reaching several hundred meters below the water level in a complex cave system. With this in mind, it is necessary to formulate some assumptions that constrain the design process.

1. Provided thrust in reverse operation is just as important as in forward drive
2. The geometry is design-constrained to a nominal diameter of 60 mm
3. The UUV is powered by an on-board battery cell with limited capacity
4. The water may contain foreign objects that can collide with the propeller blades

The first statement indicates that during a dive in an unknown area, an underwater drone performs mapping procedures during which reverse movement is as important as forward movement. In addition, a high reverse thrust is as important as a forward thrust during maneuvers in constrained spaces.
The nominal diameter constraint comes from the mechanical design of the UUV and represents the space reserved for the propeller assembly, including motors and bearings. During operation, the propeller motors will drain power from the main battery cell, therefore efficient operation should be prioritized. The toroidal geometry has been shown to be capable of higher efficiency than a conventional one [36] and should be used to maximize battery range during operation. The accumulation of debris within the propeller shaft poses a significant risk to the project success and is deemed unacceptable during dive operations. Consequently, strategies should be implemented to mitigate the accretion of foreign objects or avoid obstruction of the propeller shaft altogether. This directs the design towards a rim-driven geometry, as it exhibits superior performance when encountering objects passing through the propeller stage. [39]. From this, it is possible to fully define the problem as follows.
Function:
UUV propeller
Objective:
Maximize efficiency
Constraints:

1. Symmetric forward and reverse thrust
2. Nominal diameter of the propeller 60mm

Free variables:
Propeller shape

As described previously, the other assumptions at the start of this chapter lead to the design being either toroidal or rim-driven. However, an opportunity arises to describe a propeller surface driven both by annular and rim driven at the same time. To the point of writing this thesis, no known record of such a design has been documented.

3 GEOMETRY DESCRIPTION AND EVALUATION

This chapter begins by laying down the basics of the shape of a propeller and follows by utilizing various analytical tools to rigorously define procedures to evaluate propeller performance. Ultimately, a propeller surface is described in 3D CAD software reflecting the assumptions from the chapter 2.

3.1 The geometry of a rim-driven toroidal propeller

This derivation will follow the method described in Section 1.1 however, to avoid complicated rake and skew descriptions, the center line will be used as the blade reference line, and all the cylindrical sections centers lie on this curve. Assume a general curve γ that begins and ends at the rim at $r = r_{rim}$. For the rest of this thesis the center line will be assumed to be a quadratic curve extending inwards from the rim with its vertex at a radius of r_{hub} and terminated at the intersection with the rim, thus the end points of the center line define a center line span angle of χ. Note that different shapes of the center line do have an effect on the performance of the propeller. However, for the purposes of this work, only the quadratic shape will be considered [1], the angle χ will remain as a parameter to optimize. The following figure depicts the definition of the parameter χ in Cartesian coordinates:

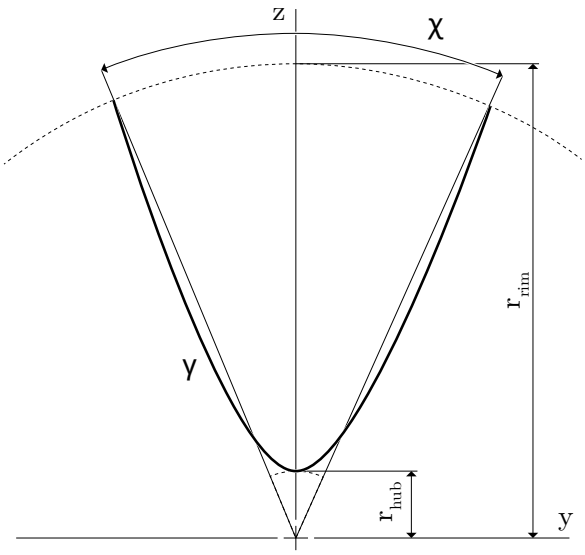

Figure 3: Blade center line

The next design parameter of the blade surface arises by accounting for the stagger of the blades to achieve the tandem propeller effect described by Liyu YE in [40]. Thus, to create the stagger, the center line is rotated about the local z axis shown in Figure 3 (or Figure 6) by an angle of ψ. The center line can be then described in Cartesian coordinates

[1] Other feasible shapes include bi-cubic, general polynomial and elliptic

as a parabola with the shape of:

$$z_{(y)} = \frac{r_{rim} \cdot \cos(\frac{\chi}{2}) - r_{hub}}{r_{rim}^2 \cdot \sin^2(\frac{\chi}{2})} y^2 + r_{hub} \tag{13}$$

and

$$x_{(y)} = y \cdot \tan(\psi) \tag{14}$$

Using a parametric curve description of the center line in a 3D space:

$$\gamma[x; y; z] \, \forall t \in < 0 \, ; \, r_{rim} \sin(\frac{\chi}{2}) >: \left[t \cdot \tan(\psi) \, ; \, t \, ; \, \frac{r_{rim} \cdot \cos(\frac{\chi}{2}) - r_{hub}}{r_{rim}^2 \cdot \sin^2(\frac{\chi}{2})} t^2 + r_{hub} \right] \tag{15}$$

It should be noted that the limits are between $t = 0$ and $t = r_{rim} \sin(\frac{\chi}{2})$ which corresponds only to one-half of the blade to counteract the discrepancies in the inflection point at $[0; 0; r_{hub}]$. To satisfy the first constraint in Chapter 2 the full blade center line can then be constructed by mirroring the half blade about the z axis (with slight variations described in Section 3.4) .
Also, note that the radial distance from the center corresponds to the Euclidean norm:

$$r_{(t)} = \sqrt{x^2 + t^2 + z_{(t)}^2} \tag{16}$$

Where $z_{(t)}$ is the z coordinate on the curve described in eq. 15

The incident fluid velocities in the propeller plane are conventionally labeled as u, v, w with respect to v_x, v_y, v_z accordingly. [15] Then the values of the components are:

$$u = u_{ax} \tag{17}$$

$$v_{(t)} = 2\pi r_{(t)} \frac{n}{60} \tag{18}$$

$$w = 0 \tag{19}$$

Where u_{ax} is the axial velocity and n is rotation frequency in RPM. It should also be noted that the velocity component z is not assumed as in ideal conditions there should be no radial acceleration of the incompressible fluid in a ducted hydrodynamic propeller [14]. The value of u remains subject to further analysis in Section 3.3.
Let there be a local directrix (direction) always tangent to γ as a normal to all blade sections labeled $\hat{\gamma}$ and defined as:

$$\hat{\gamma} = -\frac{(0; 1; \frac{\mathrm{d}z_{(t)}}{\mathrm{d}t})}{\sqrt{1 + \frac{\mathrm{d}z_{(t)}}{\mathrm{d}t}^2}} \tag{20}$$

The negative sign ensures a proper positive orientation when specifying the rotation of a blade section, also note that $\hat{\gamma}$ is a unit vector.
By defining the normal of all cross sections as not necessarily perpendicular to v it is

necessary to correct the value of incident velocity as a projection into the section plane as:

$$v' = v(-\hat{r} \cdot \hat{\gamma}) \tag{21}$$

The value of u remains unchanged as the local x direction does not change. Correcting the w component is also unnecessary as it is zero. There is no need to account for the rotation due to ψ as the y reference direction does not change when rotating the center line. Finally, the blade section is a closed blade profile located at the centerline and rotated at an angle of β_I as described in eq. 12 where the corrected value of v' is used in eq. 2:

$$\beta_{I(t)} = \theta'_{(t)} + \alpha_0 + \alpha_{i(t)} \tag{22}$$

Where by applying the correction to eq. 2:

$$\theta'_{(t)} = arctan\left(\frac{u_{ax}}{v'_{(t)}}\right) \tag{23}$$

The correction is visually interpreted in Figure. The chord length c is any function $c_{(t)}$

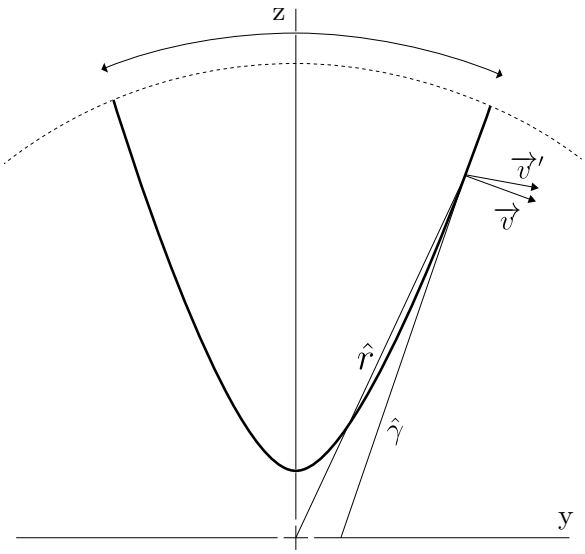

Figure 4: Velocity correction

that is smooth in the bounds of t. For the entirety of this work, assume that the chord length is linear with respect to t ranging from c_{hub} at $t = 0$ to c_{rim} at the upper bound of t.

An alternative approach can be chosen, where the cylindrical section can be defined using a line connecting a particular point of the center line with the x axis and a plane normal to this line. An analogous approach to the one discussed in Section 1.1 can be taken to counteract discrepancies caused by the surface rotation ψ. When t approaches 0, the center line itself starts to act as a blade section, near the inflection point, the blade center line aligns tangentially with the streamlines. In this region, it begins to function as a

cylindrical section on its own, leading to assumptions that $\psi = \beta_I + \alpha_0 + \alpha_i$ should be chosen to contribute to the generation of lift at the vertex. However, this would lead to surface smoothness problems, and the impact on lift and drag at small values of r becomes minimal, as can be seen from eqs. 18 and 4 (5). The method outlined earlier in this chapter was selected because it accommodates diverse changes along the center line while simultaneously ensuring a seamless blade surface throughout the curve, resulting in a blade without edges or discontinuities in any direction.

3.2 Performance assessment tools

Various tools can be used to assess propeller performance, ranging from experimental methods to the utilization of a CFD code to simulate the flow in the propeller stage. It is most logical to begin with the least time and resource-demanding options to obtain insight into the sensitivity to changes in design parameters. The blade element method can be utilized to create a simplified model of the propeller blade and geometries can be easily compared with each other. This trend is later used as input for a parametric study of propeller performance using commercial CFD code.

3.2.1 Blade element method

The blade element method (abbreviated BEM) is a discretization method where the blade is sectioned into a number of elements throughout the center line, each section contributing a differential amount to the final thrust and moment of the blade as a whole. Additional metrics such as efficiency can also be computed in this way. The description of the blade element method will closely follow the methodology laid down by A. Ghoddoussi [18] however, multiple additional effects must be taken into account due to a toroidal rim-driven geometry. In addition, the effect of ψ is not taken into account in this model, as it does not inherently change the orientation of the blade sections, but rather their interaction in wake and turbulent structures. This analysis is carried out using CFD code.

The lift and drag of a blade section is calculated using the airfoil lift and drag formula (as in eq. 4):

$$L = \frac{1}{2} C_L \rho v^2 c t \tag{24}$$

Where t is the blade length and v is the incident velocity. [24] To account for two components contributing to the incident velocity and post-differentiation with respect to t:

$$dL_{(t)} = \frac{1}{2} C_L \rho (u^2 + v^2) c_{(t)} dt \tag{25}$$

$$dD_{(t)} = \frac{1}{2} C_D \rho (u^2 + v^2) c_{(t)} dt \tag{26}$$

The following figure will be utilized to derive the formulas for propeller thrust and moment: Thrust of a blade section is generated normal to it's chord line according to the expression for the axial component $dF_{x(t)}$:

$$\mathrm{d}F_{x(t)} = \mathrm{d}L_{(t)} \cos(\beta_{I(t)}) - \mathrm{d}D_{(t)} \sin(\beta_{I(t)}) \tag{27}$$

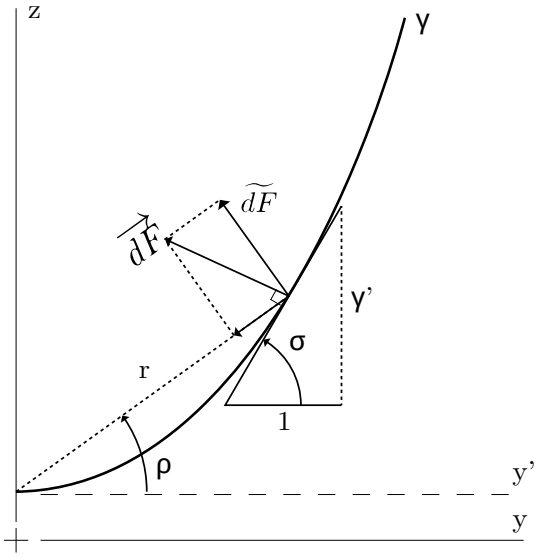

Figure 5: Blade forces

Now observing figure 5, to obtain a component of forces perpendicular to the radial coordinate $\hat{r}$ firstly, the value of $dF_{(t)}$ needs to be calculated, thus:

$$\mathrm{d}F_{(t)} = \mathrm{d}D_{(t)} \cos(\beta_{I(t)}) + \mathrm{d}L_{(t)} \sin(\beta_{I(t)}) \tag{28}$$

The component of the force normal to $\hat{r}$ is labeled as $\widetilde{\mathrm{d}F}$ is at an angle of $\rho - \sigma$ to $\overrightarrow{\mathrm{d}F}$. Where:

$$\rho = \arctan(\frac{\gamma_{z(t)}}{t}) \tag{29}$$

and:

$$\sigma_{(t)} = \arctan(\frac{\mathrm{d}z_{(t)}}{\mathrm{d}t}) \tag{30}$$

Then the differential moment $dM_{x(t)}$:

$$\overrightarrow{\mathrm{d}M_{x(t)}} = \overrightarrow{\mathrm{d}F_{(t)}} \cos(\rho - \sigma) \times \overrightarrow{r_{(t)}} \tag{31}$$

Finally the values of thrust and moment:

$$T = \kappa\, 2B \int_0^{r_{rim} sin(\frac{\chi}{2})} dF_{x(t)} \tag{32}$$

$$M_x = \kappa\, 2B \int_0^{r_{rim} sin(\frac{\chi}{2})} dM_{x(t)} \tag{33}$$

Where κ is an empirical correction factor to account for losses not governed by the model. Note that the bounds of the integral are only set for one half of the blade for reasons described above.

3.2.2 Advance ratio

The propeller advance ratio is a metric used to characterize a propeller in the latter chapters. It is defined as the relationship between the forward velocity of the vessel and the rotation velocity of the propeller at the outer diameter. Therefore:

$$J = \frac{u}{nD} \tag{34}$$

The vessel velocity definition is applicable to large ships and aircrafts, where the propeller stage axial velocity matches the longitudinal velocity of the vessel. For tugboats that experience stalling or applications where the axial velocity through the propeller stage does not match the craft velocity, the relationship is modified to represent the actual velocity at the propeller stage. [14] By modifying eq. 34 to reflect the assumptions, the formula used for propeller advance ratio will be:

$$J = \frac{2u}{nr_{rim}} \tag{35}$$

The value of J ties the axial velocity ($u = u_{ax}$) to the rotation speed of the propeller. The geometry depends on both, and as can be found in earlier chapters, the propeller angles can be deduced from the value of J for various operation settings such as different nominal angular velocity of the propeller. In the case of this problem, the axial velocity in eq. 35 denotes the x component of the velocity of the fluid passing though the propeller stage. There are methods to approximate the value of the induced axial velocity in the propeller, one of them described in Section 3.3.

3.2.3 Efficiency

To assess the performance of the propeller, the most important metric used will be its efficiency, as energy is limited on bard of an UUV, it is imperative that the design with the highest efficiency is chosen to minimize for losses. High-efficiency designs are also valuable in long-distance freights where even a minimal reduction in consumption translates into great savings in both economical and environmental factors. To begin the derivation of a propeller efficiency assume the law of conservation of energy as stated in [20]:

$$\dot{m}_1 h_{Tot1} + \dot{m}_2 h_{Tot2} + P_w + P = 0 \tag{36}$$

Where P_w is flux of thermal power, which can be neglected as heating of the medium is not assumed
h_{Tot} is total enthalpy as:

$$h_{Tot} = U + \frac{p}{\rho} + \frac{1}{2}u^2 + gz \tag{37}$$

The control volume of the duct and the propeller must satisfy the continuity equation and as the duct remains of constant cross section ($\dot{m}_1 = \dot{m}_2$) then eq. 36 becomes:

$$P = \dot{m}\Delta h_{Tot} \tag{38}$$

With positive power delivered by the motor unit. Then from eq. 37 the value of Δh_{Tot}:

$$\Delta h_{Tot} = (U_2 - U_1) + \frac{p_2 - p_1}{\rho} + \frac{u_2^2 - u_1^2}{2} + g\Delta z \tag{39}$$

The first and last term in eq. 39 cancel to zero as there is no change in internal energy or elevation. Also, the third term is zero as continuity requires $u_1 = u_2$ (by defining the control volume on the entire cross-section of the duct) and then eq. 38 becomes:

$$P = \dot{m}\frac{p_2 - p_1}{\rho} \tag{40}$$

The propeller thrust can be modeled as the action of pressure on the propeller plane [14] (see section 3.3) and thus from the definition of force

$$\Delta pA = T \tag{41}$$

Rewriting $\dot{m}$ as $A\rho u$ in eq. 40 yields

$$P_{out} = uT \tag{42}$$

Equation 42 is the expression for the effective output power of the propeller, in other words the "hydraulic" power supplied to the fluid. The input power required to rotate the blades comes from the moment in eq. 33 that resists rotary motion:

$$P_{in} = M_x\omega \tag{43}$$

Then the efficiency of the propeller can be described as:

$$\eta = \frac{P_{out}}{P_{in}} = \frac{uT}{M_x\omega} \tag{44}$$

Note that efficiency does not depend directly on the advance ratio; however, variations in J cause changes in the propeller angles and thus the induced velocity u. In propeller applications, the graphs that describe its performance are often $J - \eta$ relationships that represent the optimal operating conditions. Each screw design shows maximum efficiency at a given advance ratio. This is the best setting to operate the propeller.

3.3 Momentum theory

The description of a geometry and a numerical model requires the axial velocity to be a known parameter entering the calculation. Before proceeding with simulations, the value of u can be estimated using the Rankine disc actuator model, as explained by John Carlton [14]. The approach is based on simplifying the propeller into an infinitely thin disc that has no slip. The method is equivalent to a blade stage with an infinite number of blades. The fluid in the actuator disc absorbs all the power delivered to the disc (propeller) and converts it to the kinetic energy of the fluid volume. The following derivation has been carried out by J. Gordon Leishman in his work [24]. The reactive force from accelerating the fluid can be obtained from Newton's second law and is equivalent to thrust of the propeller:

$$T = \dot{m}u \tag{45}$$

Where u is the slipstream velocity far downstream. By defining a control volume to encompass contracting the slipstream rather than the entire cross-section of the pipe, then from energy conservation laws, a relationship between the slipstream and propeller stage velocities can be easily derived:

$$u' = 2u \tag{46}$$

The difference between the conclusions from eq. 39 and here, lie in different control volumes assumed. In section 3.2.3 it is assumed that the control volume is the entire

cross section of the duct, here only the streamline is encompassed by the control volume. Thus, to satisfy continuity, it is clear that the downstream flow must contract. For the following derivation, A' and u' are values at the venna contracta.
By substituting for u' in eq. 45 and expanding $\dot{m}$:

$$T = 2\rho A' u^2 \tag{47}$$

Then by substitution of T from eq. 42 and expressing the axial velocity an expression for induced axial velocity from power delivered can be obtained:

$$u = \sqrt[3]{\frac{P}{2\rho A'}} \tag{48}$$

Thus the axial velocity can be calculated using the effective power of the driving motor. This is useful for preliminary analysis carried out using the blade element method, where induced velocity is used as input for calculations. Also, as seen in section 3.1 the geometry of the propeller is directly influenced by the expected axial velocity. As commonly used in applications, this will be carried out by holding the rotational frequency constant and variations in advance coefficient will serve as a design parameter.

3.4 Cross section

The aerodynamic performance of a rotating blade system is significantly influenced by the geometry and flow dynamics, especially when considering annular flow reversals. As the fluid passes the inflection point, the leading edge of the blade becomes the trailing edge, and the trailing edge becomes the leading edge. This occurs due to the annular geometry of the center-line, which causes the flow direction across the inflection point to reverse, resulting in different drag and lift coefficients for forward and reverse flows. By assigning C_{L1}, C_{L2} to froward and reverse setting respectively, C_{D1}, C_{D2} for coefficients of drag. With this in consideration the values of Thrust and drag in eqs. 32 and 33 are modified to a sum of partial additions to the overall thrust by parts of the blade as:

$$T = B\int_0^{r_{rim}sin(\frac{\chi}{2})} dL_{1(t)}\mathrm{d}t + B\int_0^{r_{rim}sin(\frac{\chi}{2})} dL_{2(t)}\mathrm{d}t \tag{49}$$

$$M_x = B\int_0^{r_{rim}sin(\frac{\chi}{2})} dM_{1(t)}\mathrm{d}t + B\int_0^{r_{rim}sin(\frac{\chi}{2})} dM_{2(t)}\mathrm{d}t \tag{50}$$

As eqs. 25 and 26

$$dL_{1(t)} = \frac{1}{2}C_{L1}\rho(u^2+v^2)c_{(t)}dt \tag{51}$$

$$dD_{1(t)} = \frac{1}{2}C_{1D}\rho(u^2+v^2)c_{(t)}dt \tag{52}$$

Respectively for reverse flow parameters (index 2)
As airplanes are not designed to fly backward most airfoils are optimized for forward flow. This creates a choke point in the design process when choosing the correct airfoil. The airfoil should intuitively be x-symmetric and have zero camber. This problem has been studied by Kijung Kwon et al. [22] who experimentally investigated the lift and drag

coefficients of elliptical airfoils that are x and y symmetric, therefore generate the same thrust and drag in both forward and reverse configurations. Jean-Baptiste Marchand and colleagues [26] explored a different method by investigating the optimal NACA airfoil when oriented in reverse. Their experiments identified the NACA0021 airfoil as efficient in this configuration, providing specific values for the lift and drag coefficients. By combining both findings, it can be found that NACA 0021 performs better in forward flow than an elliptical airfoil; however, it does not outperform it in reverse operation. At this point, it is evident that the reversibility constraint burdens the design with the need to compromise between the optimal performance of the airfoil in one direction and the other. A possibility emerges then, of using a non-y-symmetric airfoil but orienting past the inflection point to operate in a reverse direction as the first half of the blade. Now, only half in reverse orientation would have its performance compromised, while the other would perform much better. Another option is to provide both halves with an elliptical airfoil to modify the performance of both halves, however, not necessarily performing worse than the backward-operating NACA airfoil. The answer to this question must be found to choose the correct option of the two. Here, the blade element method in combination with modified equations 49 and 50 can lead to an analysis of various combinations of how changes in the cross section affect the efficiency of the propeller.

3.5 CAD Model

The CAESES® CAD package was utilized to generate a robust and responsive 3D parametric model that could be integrated into an optimization task within a CFD solver. [2]

To obtain the surface of the blade, a center line was constructed as a third degree polynomial passing through the end points located on the outer run at a distance of r_{rim}, χ apart and z symmetric. The third point of the curve was located at $[x; y] = [0; r_{hub}]$ thus the center line γ was defined. The center line was then rotated by an angle of ψ discussed in Section 3.1. For each point $P[x_P; y_P; z_P] \in \gamma$ a plane π was constructed such that all unit vectors $\hat{p}$ of the connector of P and the x-axis $\overrightarrow{p} = (0; y_P; z_P)$ are normal to π. In each position t along γ the cross section was constructed in the corresponding plane $\pi_{(\gamma)}$ with a length of $c_{(t)}$ discussed in 3.1 and rotated by an angle of $\beta_{(t)}$ about $\hat{p_{(t)}}$. Note that $\beta_{(t)}$ is not a function of ψ, and therefore does not change the cross-sectional alignment. The surface is then obtained by sweeping the cross section through all positions on the center line. Figure 6 serves as a visual representation of a formation of a single cross section:

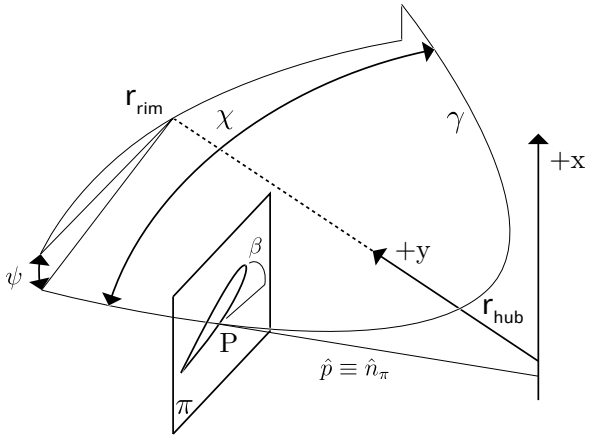

Figure 6: Cross section modeling

The trailing edge was also rounded using a fitted arc to minimize sharp edges in the model and to ensure a more efficient reverse flow operation.
Figure 7 is a computer rendering of an isometric view of the resultant shape with a periodical image of two more blade surfaces and a rim of arbitrary thickness.

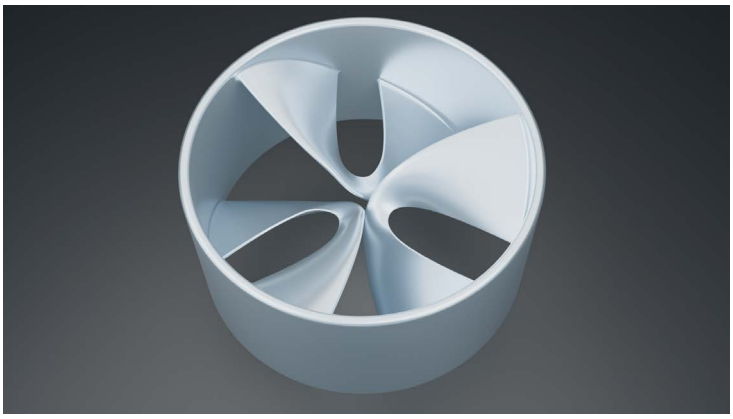

Figure 7: Isometric view of the propeller

The shape of the propeller can be uniquely defined by using multiple parameters. For the purpose of the following analysis, the surface shape has been driven by four design variables, that is,

1. Blade number B
2. Center line span angle χ
3. Center line rotation ψ
4. Advance ratio J

The chord length, characteristic angular velocity, and the radii of the hub and rim have been held constant throughout the iterative search to minimize the problem complexity.

4 DESIGN SPACE EXPLORATION

With the shape described parametrically, the natural succession in the process is to explore the performance response to changes in the parameters described in section 3.5. To achieve this, a preliminary search using a mathematical model in MATLAB has been carried out. The goal of the model was to observe the sensitivity of the model and to locate inflection points of the propeller performance curves, thus to gain approximate values to carry out more thorough investigation using more sophisticated methods such as the implementation of a commercial CFD code.

4.1 MATLAB Model

The deployment of a MATLAB model to map the response of the design has been made possible by the equations 32 and 33 derived in Chapter 3.2. It should be noted that the relative position of the cross section does not change with variations in the parameter ψ as can also be observed in Figure 6. In addition, the mutual interaction of the blades was not accounted for in the model, since no prediction of turbulent structures has been made and the number of blades could not affect the performance of the blade (to answer this, refer to chapter 1). Therefore, only the response to two of the four parameters has been analyzed, the angles χ and ψ. One of the functionalities of the model was then to observe the effect of variations in the cross section and its position on the blade, thus answering the question from section 3.4 which arrangement of cross sections proves to perform better, two elliptical profiles as suggested by K. Kwon and S. Park [22] or two NACA 0021 profiles, one in the forward and the other in reverse regime like in the studies of J.-B. Marchan et al. [26].

4.2 CFD Analysis

To obtain a more precise prediction of propeller thrust and efficiency, a commercial CFD has been utilized to iteratively quantify the performance of selected combinations of parameters obtained from the MATLAB model.

To prepare the geometry, a direct CAESES module was implemented into Ansys Workbench allowing seamless parametric optimization problems to be carried out directly inside the Workbench environment. The computational space was separated into three domains, two static cylindrical domains upstream and downstream of the propeller stage measuring $3D$ and $7D$ respectively, where D is the diameter of the propeller. The dimensions have been adopted from the approach of Ante Sikirica [34]. The central domain was rotating at the characteristic angular velocity. The interfaces between the domains were modeled using the frozen-rotor model to capture the outline of the magnitude and structure of the blade wake. The following is a visual representation of the computational domain with, in green color on the right, the inlet extension, the middle domain the rotating propeller

stage, and on the left the outlet domain. Although periodicity has been considered, the narrow band of fluid between the blade tips makes it problematic to implement without significantly affecting the stability of the solution.

Figure 8: Computational Domain

To obtain a structured mesh of the region, the Ansys Fluent meshing module was used as unexplainable complications with the native Ansys meshing software have occurred. As noted by Versteeg in his work [35], the spatial discretization should approach the Kolmogorov scale to properly capture turbulent vortices. Shown by Landahl et al. [23] the Kolmogorov scale can be obtained as:

$$\mu = \left(\frac{\nu^3}{\varepsilon}\right)^{1/4} \tag{53}$$

Alternatively, Versteeg also suggested a spatial resolution of $0.01 \cdot Re^{3/4}$ for turbulent flows. Thus, the sizing of the cells in all domains has been adjusted accordingly to ensure that the resultant flow meets the conditions. Special attention has been paid to the sizing of the blades to correctly capture the shape of the blade. The cells on the interfaces have been mapped to sizes of similar magnitudes. Eight boundary inflation layers have been introduced to the blades and three to the walls of all domains, all with a growth rate of 1.2 and a transition ratio of 2.7. To achieve a structured volumetric mesh, a poly-hexcore method was selected with one peel layer and eight buffer layers. The following are visual representations of the computational mesh (Figure 9) and a detail of the rotating domain (Figure 10).

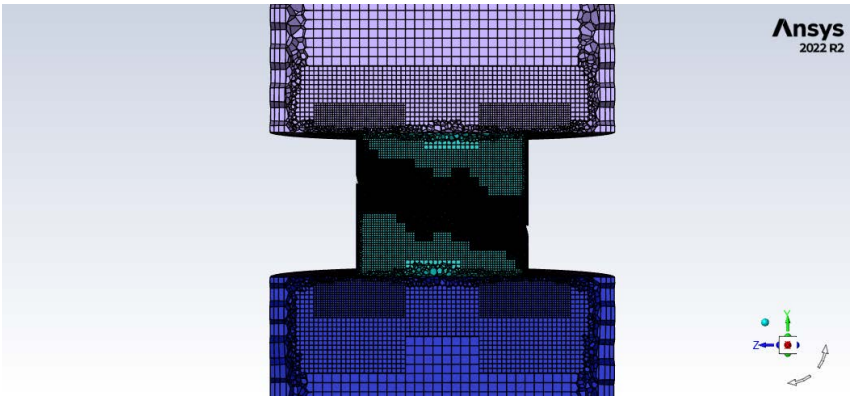

Figure 9: Mesh throughout the domains

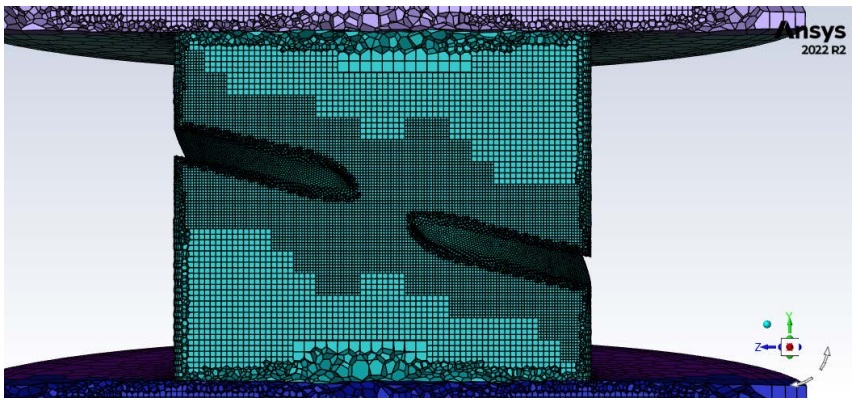

Figure 10: Detail of the rotating domain mesh

The boundary conditions have been set to zero total pressure on the inlet and outlet - the capping surfaces of the inlet and outlet cylinders, defining a zero gradient problem. This type of boundary condition is only applicable if the flow developed at the outlet boundary is steady [35], which has been proven in the solution stage.

To model turbulent behavior in a stationary problem, the $k - \varepsilon$ model or the Spalart-Allmaras model have both proven useful in practice [35]. However, some geometries have encountered divergence problems (either due to poor initialization or the choice of a turbulence model). Therefore, the designs have been validated using the SST model to ease convergence at the cost of computational resources.
Although the PISO pressure-velocity coupling method might be more efficient in general, in applications with strong p-v coupling such as a flow through a blade stage the SIMPLEC model performs comparably at a lower computational cost, therefore, it was utilized.
The simulation was stopped when the RMS residuals approached the value of 10^{-6}, however, the residual of the continuity equation was problematic with converging to only 10^{-3}. This was probably caused by the strongly transient nature of the flow captured by a stationary solution. The convergence of performance indicators such as blade moment and thrust have been monitored and converged to a stationary value over the last 1000 iterations throughout the falling residuals, at that point the solution was terminated. The Inlet-Outlet flow parity was also monitored.
In a CFD study, it is necessary to prove that the solution is not influenced by the numerical model and that the solution is not grid dependent. To verify this, it is necessary to show that the solution converges to the same value without dependence on: [35]

- Boundary condition distance
- Mesh fidelity
- Further convergence

To satisfy this, a domain with boundaries 200% further from the propeller stage was studied. To investigate the dependence of the solution on the mesh, a grid solution with an increase in cell count of 350% was carried out. The test cases have been verified within ten times larger iterations with residuals dropping lower than in the reference solution.

Throughout all test cases, the final measured thrust and moment parameters diverged by less than 0.5% of the reference solution. Thus, the solution can be proclaimed to be grid-independent and convergent. The following is a table describing the grid dependence study:

Table 1: Grid dependence study

	Inlet Distance	Outlet Distance	Blade Cell Size	Cell Count	Efficiency
Base	150mm	300mm	0.4mm	1 686 800	0.28105
Refined	300mm	600mm	0.3mm	5 894 300	0.27993

4.3 Experimental Methods

It is imperative to perform experimental validation of the CFD results to verify the model. Another use of experiments is to obtain the value of the empirical correction coefficient κ from eqs. 32 and 33 in section 3.2.1. To evaluate propeller performance, a test mount was constructed consisting of the propeller with a short (<1D) elliptical inlet on the suction side and a long (10D) tube at the outlet. The propeller ring was inserted into a carrier supported by two deep groove ball bearings. The carrier was driven by a BLDC motor and the motion transmitted with a timing belt a schematic is depicted in figure 11. The assembly was submerged in a confined space of 1x1x0.5m of water to achieve immersion of the propeller, while leaving enough space downstream to allow regeneration of the current and its stall before recirculation. Additionally, it has been shown experimentally that using a suction duct or an outlet diffuser had no effect on the measured performance, therefore they have not been utilized during the measurements.

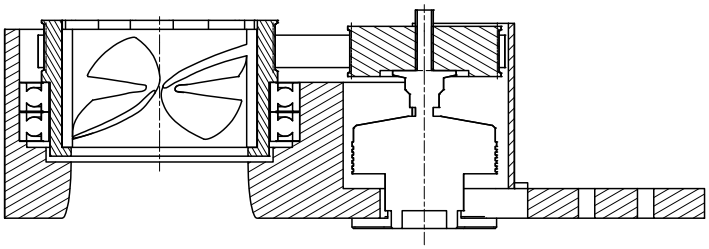

Figure 11: Testing Module

The rotational speed was measured using real-time feedback from the electronic speed controller (ESC) through an Arduino logging the serial signal. The power values were measured using a voltmeter and an amp meter connected to the battery lines. To obtain the thrust measurement, the setup was mounted on a tensometric plate through the mounting port on the right in Fig. 11. More details on the experimental procedure can be found in Section 5.3.

5 RESULTS AND DISCUSSION

The subsequent sections detail the results and insights derived from the analysis methods previously outlined. This study primarily aimed to optimize the propeller geometry, with considerable focus placed on "exploring" the design parameter space due to the novelty of this proposed propulsion model. Therefore, in addition to identifying maximum efficiency within the parameter space, a comprehensive approach was employed to assess the influence of individual parameters on the propeller's resultant flow and performance.

5.1 BEM Models

To address the questions raised in section 3.4 equations 49 and 50 have been implemented in a discretized form. Initially, to validate the concept of an annular center line, two models have been assessed, one with an annular center line described by eq. 15 and other with a linear center line of:

$$\tilde{\gamma}[x; y; z] \forall t \in < r_{rim}; r_{hub} >: [t; 0; 0] \tag{54}$$

leading to a modified variant of eq. 49:

$$T = \kappa \, B \int_{r_{hub}}^{r_{rim}} dF_{x(t)} \tag{55}$$

Where $\mathrm{d}F_{x(t)}$ excludes the χ parameter. By graphing the performance metrics for both a linear and a toroidal center line propeller across various angular speeds:

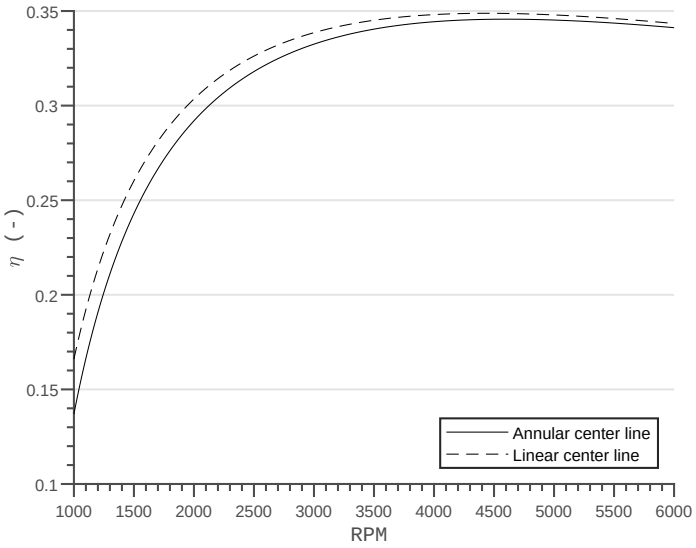

Figure 12: Center line shape comparison

As shown in Figure 12, the variation in efficiency is minimal when comparing the designs of the annular and linear center lines. However, it should be kept in mind that the motivation

behind introducing the annular design was to mitigate tip vorticity effects not accounted for by this approach (other than in κ).It is important to examine the different variations introduced in section 3.4, which outlines two suggested cross sections; one elliptical and the other NACA 0021. To identify the variant that is more efficient, two BEM models have been compared with different values of lift and drag coefficients that model the two cross sections, the values have been adopted from [22] and [21].

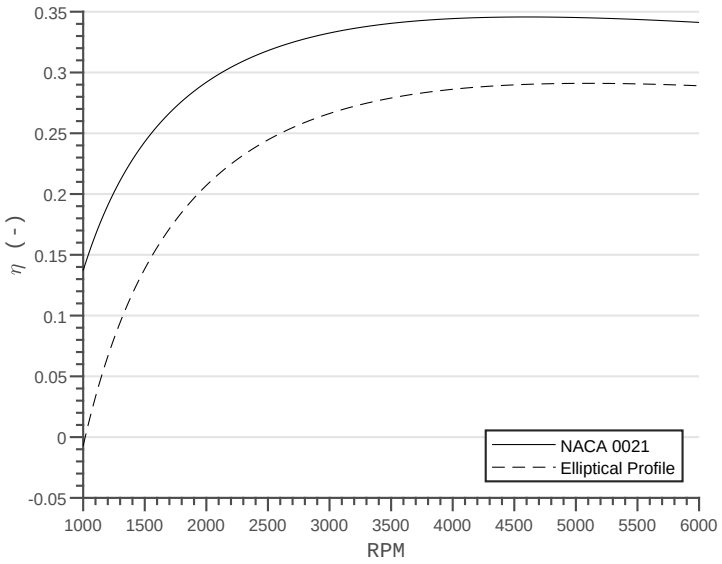

Figure 13: Cross section selection

Figure 13 shows the NACA 0021 profile results in a more efficient design despite the fact that half of the center line is oriented in reverse flow configuration. For this reason, the rest of the analysis will only be considered with a center line of a NACA 0021 profile. This assumption was also valid when constructing Figure 12.
From both figures, it can also be observed that the $\eta - n$ characteristic has a maximum and thus an effective operation point in which efficiency is the highest.
By sweeping the range of possible values of the parameter χ at a constant angular velocity, it was found that the value of χ has no effect on the resulting efficiency at a given rotational speed. This conclusion is intuitive, as the orientation of the cross sections does not vary nor does the center line length. Note that this model does not assume any turbulent interaction between the blades, which may have a large impact on the choice of χ and it would be wrong to assume that the design does not respond to changes in χ.

5.2 CFD Analysis results

To deepen the understanding of the behavior of the toroidal rim thruster geometry, an approach using CFD tools was utilized to model turbulent behavior of the flow at the propeller stage, granting insights into the interaction of the propeller blades, possibly on the choice of χ. Following the description of the model in Section 4.2, an iterative procedure has been chosen to acquire the resulting values. The model has been calculated for different combinations of χ, J, and ψ to capture the characteristics across all potential values. Since the method involved an iterative process with various parameter ensembles to define the problem, a computational cluster was employed to carry out the solutions in a shorter time. The flow chart in Figure 14 describes the algorithm used to obtain each solution in a combined setup using a local machine to define the problem and a remote HPC to solve the flow equations using a commercial CFD code (Ansys Fluent).

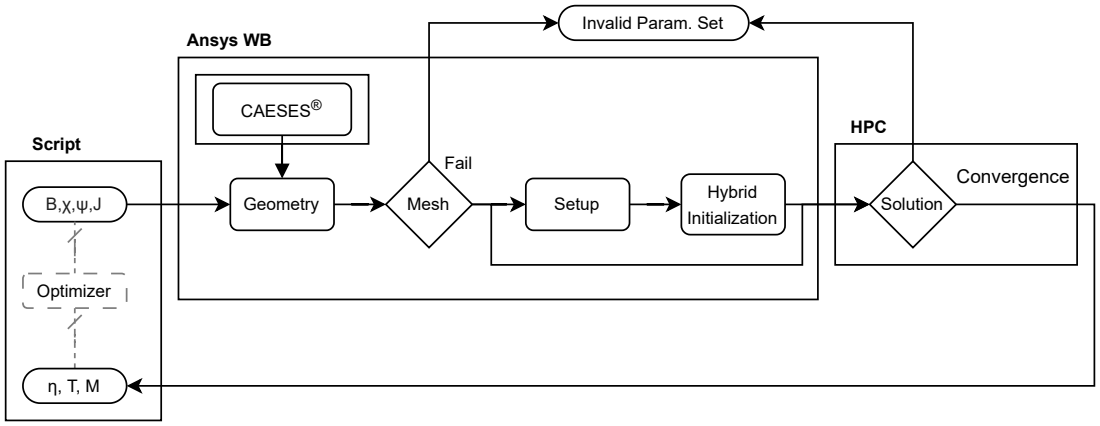

Figure 14: Iterative solution algorithm

As mentioned in previous chapters, the design is fully defined using a set of parameters, specifically: $r_{hub}, r_{rim}, c_{hub}, c_{rim}, B, \chi, \psi, J$. The first four parameters were kept constant during the response study and only B, χ, ψ, J was modified to simplify the complexity of the problem. To obtain a full response study, more research is needed on the sensitivity to changes in $r_{hub}, r_{rim}, c_{hub}$ and c_{rim}. For this specific scenario, the input variables have been entered into the Ansys workbench, where the CAESES plug-in was used to convert them into a domain featuring the desired propeller. Subsequently, this was processed through the Fluent meshing algorithm to generate a mesh with dimensions that match those of the reference mesh detailed in Section 4.2 to maintain consistent spatial resolution. In case the mesh resulted in an error, due to blade intersection or other reasons, this parameter was labeled invalid, and solution was not obtained at this point.Upon the successful completion of the meshing process, the case was set up in Ansys Fluent under consistent conditions and was initialized using the integrated hybrid solver. The case and mesh data have then been uploaded to a high-performance cluster where the Fluent solver has been utilized to run 5000 iterations, or until convergence criteria are satisfied (sec. 4.2) to obtain the results. Those were later extracted from the solver logs and downloaded back

onto the local machine that stored the performance values of the specific design. At this point, to find the next set of input parameters, an optimization algorithm could have been possibly utilized until the process converges to a specific design, had the sole purpose of the exercise been to obtain a maximum efficiency and not to conduct a response study. It should also be noted that the values of Section 5.1 can be used as initial conditions for the optimization algorithm. Note that a gradient-based search should not be utilized in this case, as the exact solution value is strongly affected by numerical diffusion, and the sampling points should be farther apart. Simplex methods or Bayesian algorithms might prove to be more effective.
Figure 15 features a comparison of the geometries chosen in the first row in the order from left to right described in Table 2. The table describes the geometry using parameters as defined in Chapter 3 and also includes performance characteristics that provide further information on the operation of the propeller. It is visible from Table 2 that while designs C and B produce a higher thrust, design B is more efficient. An insight into a possible explanation is discussed later in this chapter and depicted in Figure 17.

Table 2: Featured variations

Column	**Design A**	**Design B**	**Design C**
$J\,[-]$	0.84	0.75	0.8
$\psi\,[\text{deg}]$	30°	55°	30°
$\chi\,[\text{deg}]$	50°	50°	60°
Performance	**Design A**	**Design B**	**Design C**
$\eta\,[-]$	0.30	0.28	0.31
$T\,[\text{N}]$	50 [N]	40 [N]	54 [N]

The middle row in Figure 15 shows the values of absolute pressure on the blades with a reference boundary pressure of $100\,kPa$[1]. The white pockets represent regions with pressure below the saturated vapor pressure at the given conditions, therefore regions with cavitation risks. Those areas will disappear at drafts exceeding $2\,m$, which is expected for submarines or even for many marine uses. Therefore, the risk of cavitation is minimal if adequate precaution measures are taken during operation at the water surface. The third row shows the axial velocity field in the stationary frame with vectors of velocity as black arrows.

[1]Although the solution has been obtained for $0\,Pa$ boundary total pressure, for visualization purposes the pressure field has been offset by $+100\,kPa$

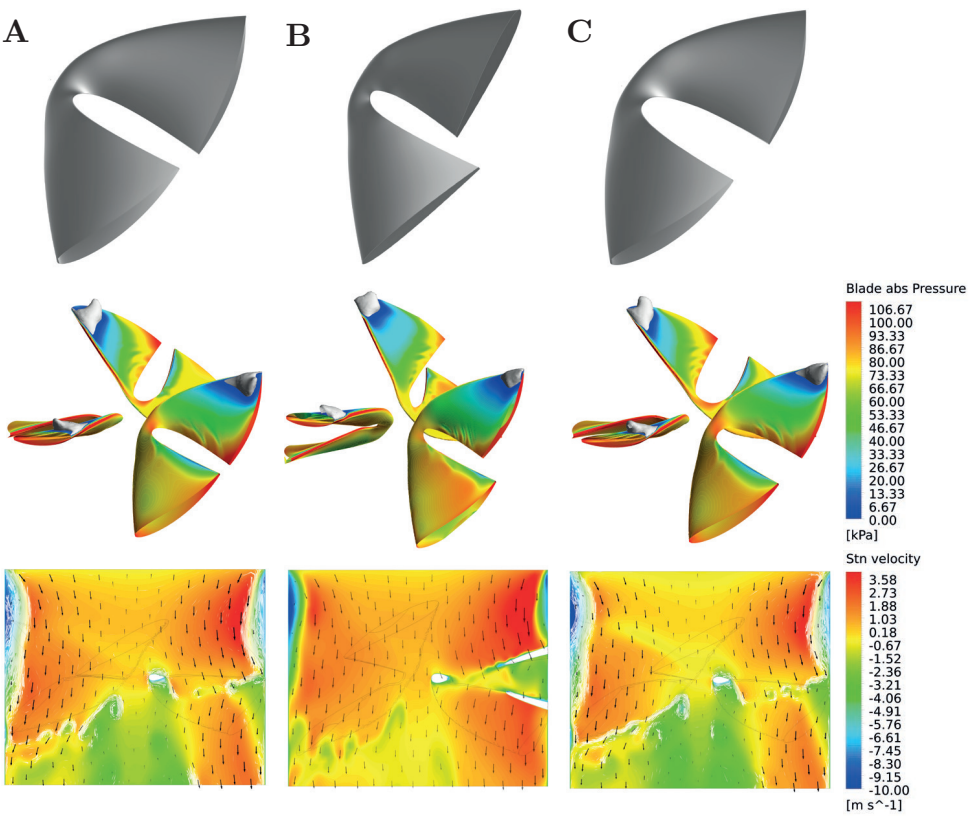

Figure 15: Effect of geometry variations

A closer look at the transition point of the blade offers insight into the underlying mechanics of toroidal geometry. Figure 16 shows a detailed view of the blade and an iso-surface of 60 kPa.

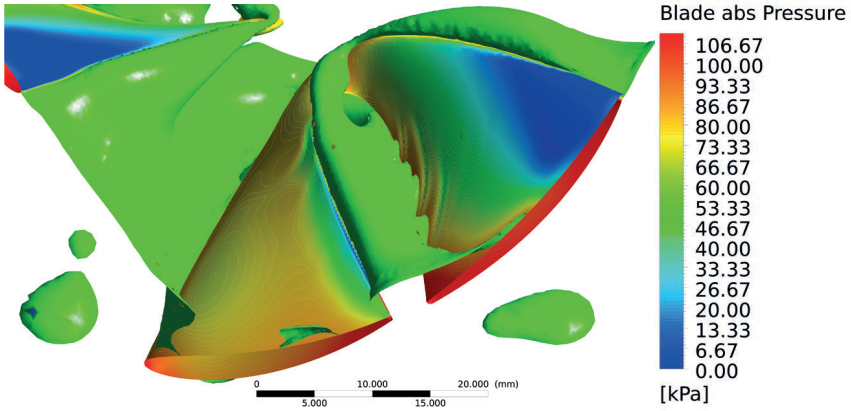

Figure 16: Transition detail

It can be seen how the low-pressure zone travels across the blade surface toward the trailing edge through the transition (inflection) point and creates a low-pressure region behind the first blade of the two-part blade series. Due to this effect, the downstream blade is located partially in the wake of the upstream blade, affecting the pressure distribution on the

downstream blade, as visible in Figure 16. This would suggest that the ideal arrangement of the blades using the parameters ψ and χ would be such that the downstream blade is located outside the wake region rather than in a close configuration of the blades. It seems that ideally, the geometry should aim to feature two blades spread apart with proper stagger such that the blades minimize each others interaction and the transition point serving as a region guiding the wake to the trailing edge while minimizing vortex sheet detachment. Forwarding the wake of the upstream blade directly to the leading edge of the downstream blade is not an ideal arrangement leading to a decrease in performance. Additionally, Figure 16 reveals the formation of high-pressure leakage zones on the suction side of the blade near the trailing edge. Those zones are most likely transient artifacts of vortex shedding from the trailing edge. This could be addressed by introducing bioinspired ridge features on the trailing edge, similar to the ones studied by Jie Yang et al. [38] or by disrupting the vortex structures of the leading edge using tubercles as studied by Max Hieke et al. [27]. To better visualize the turbulent sheet propagation downstream the blade arrangement, Figure 17 shows flow helicity[2] contours of two cylindrical shells at radii 25 mm and 6 mm for two variations of designs referenced in Table 2. It is visible how the mutual blade position affects the magnitude and propagation of the vortex structure.

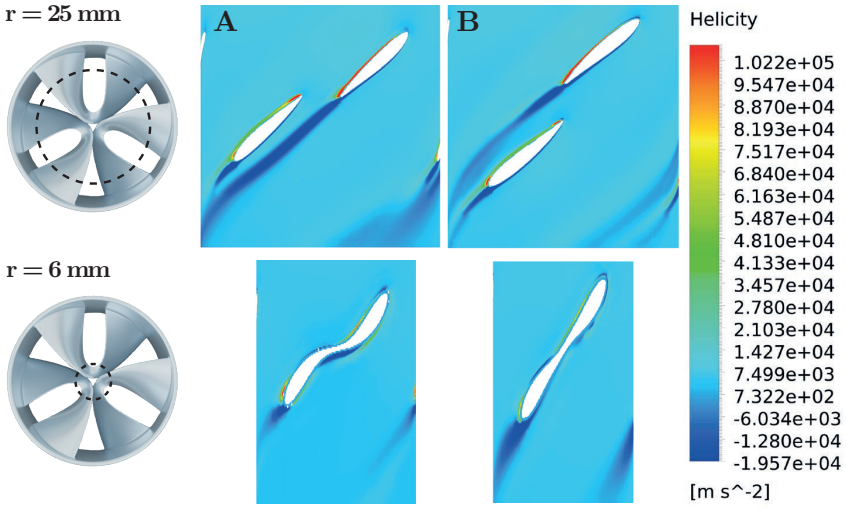

Figure 17: Helicity contour

Upon comparing the contours of Figure 17 with Table 2 it can be observed how the wake region can affect the performance of the propeller. The proper position of the blade significantly affects the performance of the geometry of the tandem blade, where the performance of the downstream blade is influenced by the wakes of the upstream blade. The wake of the upstream blade might be forwarded either to the pressure or suction side of the downstream blade. It should be noted that both the A and C geometries of Table 2 (Fig. 15) position the upstream blade so that the wake region is forwarded to the pressure side; see Figure 17-A. It can be seen that those two variants (and more not visualized

[2] An analogy to swirl strength defined as: $H = \int_V \vec{u} \cdot (\nabla \times \vec{u}) \mathrm{dV}$ [13]

here) have shown superior thrust and efficiency characteristics compared to geometries that evacuate the trailing vortex below the pressure side, see Figure 17-B.

Thirty variations of the input parameters have been studied, dispersed throughout the design space guided by the intermediate results. As the characteristic chart would be complete in a 4D space, various sections have to be visualized to comprehensively present the results. In each cross section of the design space, the maximum values should be representative of the impact on the final design. The values with the lower efficiency values might be a trace of a different change visible on other figures (an axis not visible in the figure). Unless the values are solitary or at either end of the variable range, the lower than maximal values should be influenced by other changes than the ones visible in the figure. Firstly, sensitivity to χ was studied in Figure 18:

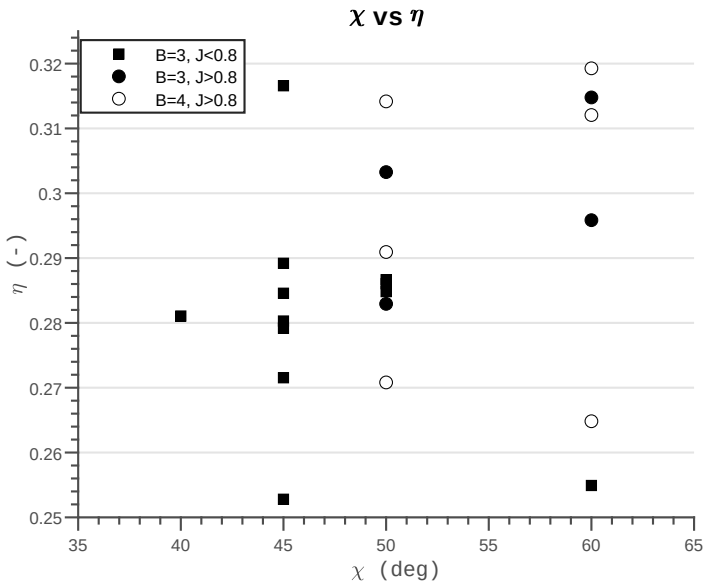

Figure 18: χ characteristic

Traces of other parameters are depicted using various symbols; designs with higher blade number (four) are marked in white, whereas three-bladed geometries are marked black. The circles show traces of geometries with advance ratios over 0.8 and the squares are geometries with $J < 0.8$. The study does not suggest that the geometry does not respond to a specific value of χ much better than others. The lower points are traces of other geometries that have been varied in other ways than by changes of χ. This coincides with the findings of the BEM analysis. A parameter that could not be studied using the BEM method was ψ, the following figure shows the results of the more sophisticated CFD approach:

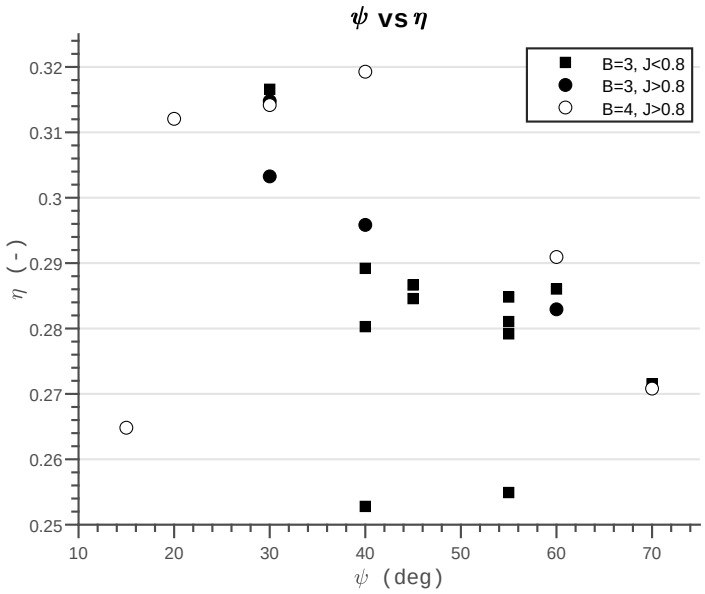

Figure 19: ψ characteristic

In this view, it seems that the designs with a higher blade number (white markers) performed better compared to three blades. In addition, a characteristic sensitivity can be observed on the graph and the fact that the design has a maximum efficiency at $\psi \approx 40°$. The description is finalized in the final view with a response characteristic to changes in advance ratio:

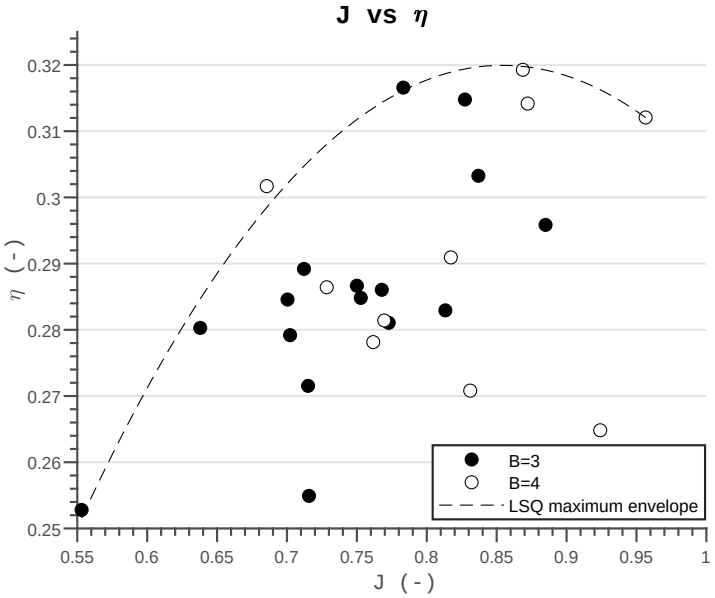

Figure 20: J characteristic

Here, the maximum envelope of the points is shown using an interpolated parabola. From this view, it is not evident whether the higher blade number does or does not impact

the performance, as a fair amount of other designs have approached the results of the four-bladed variations. Individual maximum points have been fitted with a second-order polynomial using the least squares method. The envelope has physical grounds, as often the performance curves of propeller geometries resemble a parabolic curve. [14] The characteristic takes the shape of the performance curves of smaller Ka-Series propellers at higher nominal rotational speed. [29] It is also clear that the results from the BEM model have slightly overestimated the performance curve; this is mostly due to the addition of turbulent interaction between the blades. The study cannot confirm the impact of the choice of ψ and χ values such that the resultant geometry features streamline surface and the flow transitions from one half-blade onto another. Neither was it possible to find correlations with the theory that the staggering of the blade sections or aligning them onto one streamline has a significant effect on the results.

5.3 Experimental validation results

The experiments were carried out following the methods discussed in section 4.3. The tensometric unit was mounted to a rod that extended from the port in Fig. 11. Using a feed from an ESP the RPM was measured (alternatively, a DFT analysis on the tensometric measurements yielded the same results). To eliminate passive friction introduced by bearings and water resistance, measurements were taken on a ring module without any blades, followed by replacing the ring with a blade stage. The resultant power drain by the propeller blades was assumed to be the difference between the passive and active power supplied. Throughout the experiments, power measurements were taken based on the current and voltage in the battery lines leading to the ESC. Consequently, any passive losses occurring within the ESC itself were not included in these readings. This introduces an inherent error to the measurements of unknown magnitude that was neglected when analyzing the results. The thrust was measured using the aforementioned tensometric plate averaged over a duration of 10 seconds of measurement. The axial velocity at the blade stage was calculated using eq. 45 and then eq.44 to obtain the propeller efficiency. A sweep was performed through various rotational speeds; however, the BLDC motor was unable to supply enough power to reach the desired 5000 RPM for which the design was intended (and should be its BEP). The experiment still provided important feedback on the accuracy of the previous analyzes. Figure 21 shows a comparison of the results of the thrust values of various computation methods with the experimental results.

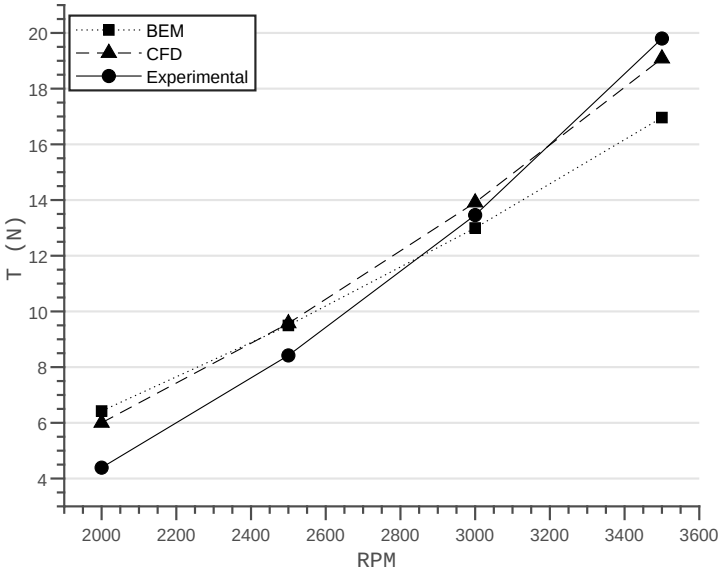

Figure 21: Thrust comparison

Figure 21 illustrates that both methods produce results closely aligning with the experimental data, with errors generally below 10%, apart from the initial data entry. The results of the BEM model resembled those derived from the CFD analyses. However, as the RPM increases, the model's predictions diverge from the experimental findings,

attributed to the impact of turbulent flow, with the CFD simulation providing a more accurate prediction of this phenomenon. In general, both computational methods effectively approximated the characteristic behavior.
To assess the efficiency values, a different propeller design with a linear center line was evaluated. Using the same method of design as described in chapter 3 but with the central line being linear, as discussed in section 5.1. Efficiency measurements were also plotted in Figure 22

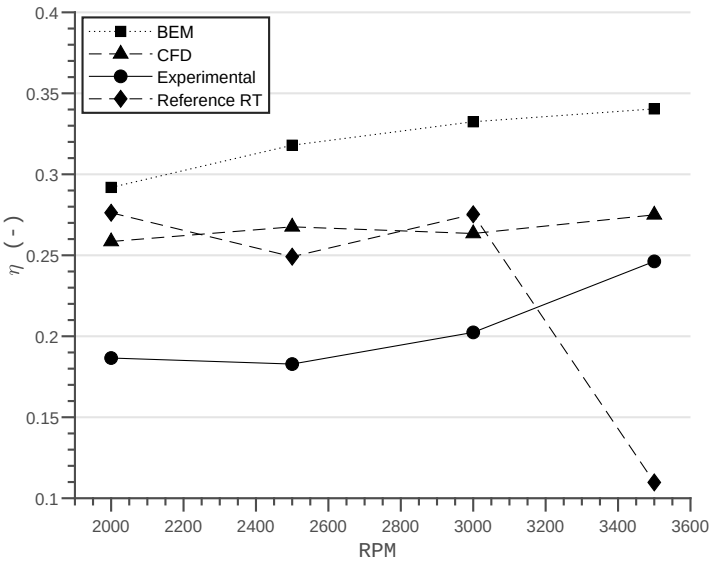

Figure 22: Efficiency Comparison

The experimental efficiency value diverges from the prediction of the computational models more significantly than when comparing thrust produced, whereas the CFD model performs better than the BEM in predicting the propeller efficiency. The margin of error was partially influenced by mechanical losses in the loaded system, which could not be measured by the empty ring, also due to additional losses in the ESC at higher loads. In the experiments, the reference Rim Thruster with a linear center line performed substantially better than its annular counterpart, which contradicts the predictions drawn from Figure 12. However, the reference thruster quickly loses efficiency at an increased RPM due to limitations in the power unit. Although the design methodology was the same and both geometries were intended to function at the same nominal rotational speed, the toroidal geometry appears to surpass the linear design at elevated speeds, particularly as the battery's power consumption rose sharply.

CONCLUSION

The theory of fixed-pitch propellers was utilized to suggest an innovative geometry that merges advancements in marine propulsion methods, specifically the rim-driven and toroidal (annular) geometries. A novel blade shape was proposed by applying the recent findings in the individual fields onto a propeller with a redefined centerline to accommodate the geometric constraints. Consequently, numerical methods (namely the BEM and Rankine models) have been used to predict the performance of the propeller in operation. A preliminary search using the two models has shown the superiority of the NACA airfoil used in forward and reverse alignment over an elliptical blade section.

Based on the analytical model, a CFD analysis was performed. At this stage, the geometry was parameterized to define the shape of the propeller, which was later used to map and identify the combinations of parameters that lead to the design with optimal efficiency from within the proposed parameter combinations. The iterative design evaluation was carried out using HPC coupled with commercial CFD evaluation and CAD geometry generation. The computational costs per iteration remained highly demanding on the local machine, therefore, only a limited design search has been carried out. To validate the CFD results, experimental trials have been conducted. The results of the trials have been used to calibrate the numerical model used in the beginning of the design process to produce results consistent with the trials and the CFD.

The analysis has shown how the transition point guides the wake region towards the trailing edge while minimizing shedding. It has been also observed that combinations of parameters that result in the blades staggering outside the mutual wake region lead to more efficient designs. In addition, geometries that clear the wake of the upstream blade through the pressure side of the downstream blade have shown superior performance to those directing the trailing vortex sheet to the suction side. Further research needs to be done to properly map out the design space and explore other variations of the proposed model. A closer inspection of the turbulent formations caused by annular tips in a podded propeller is required, which can be achieved through a transient model study and experimental measurements.

Experimental measurements have shown the toroidal rim-driven propeller is a viable alternative to present-day propeller models and conventional rim-driven propulsion. The candidate design has closely matched the performance of the rim-driven models. The new geometry has a applicable use in UUVs that are space-constrained and seek a robust, yet compact propulsion system that is resilient to debris and rope tangling the central shaft. The rim-driven geometry is capable of providing thrust at comparable efficiency to shaft propellers but in a much smaller assembly size. The design can also be used as an alternative to present-day solutions in podded thrusters, bow thrusters, and jet propulsion solutions used in maritime applications. With further development in the field, a viable configuration of the blades may be capable of exploiting the benefits of toroidal propellers and yield a geometry superior to current solutions, also benefiting from the simplicity of the assembly of the thruster drivetrain.

BIBLIOGRAPHY

[1] *Aerospaceweb.org | Ask Us - NACA Airfoil Series*. https://aerospaceweb.org/question/airfoils/q0041.shtml. (Accessed on 10/13/2024).

[2] *CAESES - CAD for Automated Shape Optimization*. https://www.caeses.com/. (Accessed on 02/07/2025).

[3] *Copenhagen Subsea A/S | Electric Subsea Thrusters | Products*. https://www.copenhagensubsea.com/products. (Accessed on 10/07/2024).

[4] *Hranická propast - speleo.cz*. https://www.speleo.cz/hranicka-propast1#:~:text=Hranick%C3%A1%20propast%20je%20zaj%C3%ADmavou%20a,kone%C4%8Dn%C3%A1%20hloubka%20nen%C3%AD%20st%C3%A1le%20zn%C3%A1ma. (Accessed on 10/06/2024).

[5] *P-04 Podvodní dron ARGO | strojLAB*. https://www.strojlab.cz/p-04. (Accessed on 10/06/2024).

[6] *Performance Reports – Sharrow Marine*. https://sharrowmarine.com/blogs/performance-reports. (Accessed on 10/06/2024).

[7] *Rolls-Royce announces delivery of first permanent magnet tunnel thruster | Rolls-Royce*. https://www.rolls-royce.com/media/press-releases-archive/yr-2012/120920-tunnel-thruster.aspx. (Accessed on 10/06/2024).

[8] *Saving lives with innovation - H2O Drones*. https://www.h2o-drones.com/en/nieuws-en/saving-lives-with-innovation/. (Accessed on 10/06/2024).

[9] *Sharrow Propeller™*. https://boattest.com/Sharrow-Propeller. (Accessed on 10/06/2024).

[10] *The Thai cave rescue is relying on some totally ingenious tech hacks | WIRED*. https://www.wired.com/story/thai-cave-rescue-boys-news-tech/. (Accessed on 10/06/2024).

[11] *Winglets | Glenn Research Center | NASA*. https://www1.grc.nasa.gov/beginners-guide-to-aeronautics/winglets/. (Accessed on 10/08/2024).

[12] Anderson, J. *Fundamentals of Aerodynamics*. 1 ed. New York: McGraw-Hill Book Company, 1984.

[13] Batchelor, G. *An Introduction to Fluid Dynamics*. 1st Ed. Cambridge: University Press, 1970.

[14] Carlton, J. *Marine Propellers and Propulsion (2nd Edition)*. 2nd edition. San Diego: Elsevier, 2007. ISBN 0750681500.

[15] Conference, I. T. T. Model Manufacture, Propeller Models Terminology and Nomenclature for Propeller Geometry. In: *ITTC – Recommended Procedures and Guidelines*. 2008.

[16] FRIEDRICH, H. *Fan*. U.S. Patent US2273756A. Sep 1939. United States Patent and Trademark Office. Available at: `https://patents.google.com/patent/US2273756A`.

[17] Gaggero, S. Numerical design of a RIM-driven thruster using a RANS-based optimization approach. *Applied Ocean Research*. 2020, vol. 94, pg. 101941. DOI: https://doi.org/10.1016/j.apor.2019.101941. ISSN 0141-1187. Available at: `https://www.sciencedirect.com/science/article/pii/S0141118719303219`.

[18] Ghoddoussi, A. *A more comprehensive database for propeller performance validations at low reynolds numbers*. 2016. Disertační práce. Wichita State University.

[19] Guerrero, J. E., Maestro, D. a Bottaro, A. Biomimetic spiroid winglets for lift and drag control. *Comptes rendus. Mecanique*. ISSY-LES-MOULINEAUX: Elsevier SAS. 2012, vol. 340, no. 1, pg. 67–80. ISSN 1631-0721.

[20] Gulich, J. F. *Centrifugal Pumps*. 3rd edition. Berlin, Heidelberg: Springer-Verlag, 2010. ISBN 3642128238.

[21] Jacobs, . *The characteristics of 78 related airfoil sections from tests in the variable-density wind tunnel / by Eastman N. Jacobs, Kenneth E. Ward and Robert M. Pinkerton ; reprint of Report no. 460, originally published November 1933*. District of Columbia: U.S. G.P.O., 1939, 1933.

[22] Kwon, K. a Park, S. Aerodynamic Characteristics of an Elliptic Airfoil at Low Reynolds Number. *Journal of Aircraft*. Jun 2005, vol. 42, pg. 1642–1644. DOI: 10.2514/6.2005-4762.

[23] Landahl, M. T., Mollo Christensen, E. a Korman, M. S. Turbulence and Random Processes in Fluid Mechanics. *The Journal of the Acoustical Society of America*. 1989, vol. 86, no. 6, pg. 2471–2471. ISSN 0001-4966.

[24] Leishman, J. G. *Principles of helicopter aerodynamics*. Second edition.; Reprinted. Cambridge: Cambridge University Press, 2008. Aerospace Series (Cambridge). ISBN 978-1-107-01335-3.

[25] Liu, B. a Vanierschot, M. Numerical Study of the Hydrodynamic Characteristics Comparison between a Ducted Propeller and a Rim-Driven Thruster. *Applied sciences*. Basel: MDPI AG. 2021, vol. 11, no. 11, pg. 4919. ISSN 2076-3417.

[26] Marchand, J.-B., Astolfi, J. A. a Bot, P. Discontinuity of lift on a hydrofoil in reversed flow for tidal turbine application. *European journal of mechanics, B, Fluids*. AMSTERDAM: Elsevier Masson SAS. 2017, vol. 63, pg. 90–99. ISSN 0997-7546.

[27] Max Hieke, M. W. a Wurm, F.-H. The influence of leading edge tubercle on the transient pressure fluctuations of a hubless propeller. In: *Proceedings of the 16th European Turbomachinery Conference*. 2025.

[28] Nechleba, M. *Vodní turbíny, jejich konstrukce a příslušenství.* 2. vyd. Praha: SNTL, 1962.

[29] Ouldhamrane, H., Charpentier, J.-F., Khoucha, F., Zaoui, A., Achour, Y. et al. Optimal Design of Axial Flux Permanent Magnet Motors for Ship RIM-Driven Thruster. *Machines*. Oct 2022. DOI: 10.3390/machines10100932.

[30] Schmirler, M. a Netrebska, H. The design of axial shaftless pump. In: *EPJ Web of Conferences*. Les Ulis: EDP Sciences, 2017, vol. 143, pg. 2104. ISSN 2101-6275.

[31] Sebastian, T. a Strem, C. *Toroidal Propeller*. U.S. Patent US20190135410A1. Sep 2020. United States Patent and Trademark Office. Available at: `https://patents.google.com/patent/US20190135410A1`.

[32] Sebastian, T. a Strem, C. *Toroidal propeller*. 2020.

[33] Sharrow, G. C. *Propeller*. Patent EP2941539A4. 2024. European Patent Office. Available at: `https://patents.google.com/patent/EP2941539A4`.

[34] Sikirica, A., Lučin, I., Čarija, Z. a Lučin, B. CFD Analysis of Marine Propeller Configurations in Cavitating Conditions. *Pomorski zbornik (Online)*. Rijeka: Croatian Association of Maritime Science and Transport. 2020, vol. 3, no. 3, pg. 251–264. ISSN 0554-6397.

[35] Versteeg, H. K. H. K. *An introduction to computational fluid dynamics : the finite volume method*. 2nd ed. Harlow: Pearson Prentice Hall, 2007. ISBN 978-0-13-127498-3.

[36] Xiang, Y. a Wang, W. Hydrodynamic performance evaluation of pump-jet propulsion based on the toroidal propeller. *Ocean engineering*. Elsevier Ltd. 2024, vol. 311, pg. 118932. ISSN 0029-8018.

[37] Yan, X., Liang, X., Ouyang, W., Liu, Z., Liu, B. et al. A review of progress and applications of ship shaft-less rim-driven thrusters. *Ocean Engineering*. 2017, vol. 144, pg. 142–156. DOI: https://doi.org/10.1016/j.oceaneng.2017.08.045. ISSN 0029-8018. Available at: `https://www.sciencedirect.com/science/article/pii/S0029801817305164`.

[38] Yang, J., Gao, H. a and, Y. Y. A numerical research on the hydrodynamic performance of marine propellers with bionic coupled blade sections. *Ships and Offshore Structures*. Taylor & Francis. 2024, vol. 0, no. 0, pg. 1–13. DOI: 10.1080/17445302.2024.2356482. Available at: `https://doi.org/10.1080/17445302.2024.2356482`.

[39] Yao, H.-D. *Pilot study of electric hubless rim-driven thrusters for transport in inland waterways*. 2023. Available at: `https://lighthouse.nu/images/Rapporter/FS24_2022_Hubless_rim-driven_propeller.pdf`.

[40] YE, L., WANG, C., SUN, C. a GUO, C. Mathematical expression method for geometric shape of toroidal propeller. *Zhongguo Jianchuan Yanjiu*. Editorial Office of Chinese Journal of Ship Research. 2024, vol. 19, no. 3, pg. 224–233. ISSN 1673-3185.

[41] ZHU, Z. a LIU, H. The external characteristics and inner flow research of rim-driven thruster. *Advances in mechanical engineering*. London, England: SAGE Publications. 2022, vol. 14, no. 2, pg. 168781322210816. ISSN 1687-8132.

NOMENCLATURE

κ	Correction factor
μ	Kolmogorov scale
ε	Turbulent dissipation energy
φ	Rake angle
H	Helicity
p	Propeller pitch
u_{ax}	Axial velocity
α	Angle of incidence
α_0	Most efficient angle of incidence
α_i	Induced angle of attack
β_I	Hydrodynamic flow angle
χ	rim center line span angle
γ	Center line
$\hat{x}$	Unit vector
ω	Angular velocity
ϕ	Directrix angle
	Center line rotation angle
ρ	Density
θ	Pitch angle
B	Blade number
c	Chord length
C_D	Coefficient of drag
C_L	Coefficient of lift
D	Drag Force, Diameter
h	Enthalpy
J	Advance ratio

L	Lift Force
M	Torque
n	Rotational frequency $[rev/min]$
P	Power
r_{hub}	Hub radius
r_{rim}	Duct radius
S	Wing area
T	Thrust
t	Wing thickness, Position parameter
u, v, w	velocity in $\hat{x}, \hat{y}, \hat{z}$
BEM	Blade Element Method
BEP	Best Efficiency Point
CFD	Computational Fluid Dynamics
ESP	Electronic Speed Controller
HPC	High Performance Cluster

LIST OF FIGURES